Piezoelectric MEMS sensors: state-of-the-art and perspectives

You may also be interested in:

Group III nitride and SiC based MEMS and NEMS
V Cimalla, J Pezoldt and O Ambacher

Fabrication and performance characteristics of high-frequency micromachined bulk acoustic wave quartz resonator arrays
Ping Kao, David Allara and Srinivas Tadigadapa

A review of piezoelectric polymers as functional materials for electromechanical transducers
Khaled S Ramadan, D Sameoto and S Evoy

Piezoelectric thin films: an integrated review on transducers and energy harvesting
Asif Khan, Zafar Abas, Heung Soo Kim et al.

Micromachined infrared detectors based on pyroelectricthin films
Paul Muralt

Biosensors: recent advances
A F Collings and Frank Caruso

Glory of piezoelectric perovskites
Kenji Uchino

TOPICAL REVIEW

Piezoelectric MEMS sensors: state-of-the-art and perspectives

S Tadigadapa[1] and K Mateti

Department of Electrical Engineering, The Pennsylvania State University, University Park, PA 16802, USA

E-mail: sat10@psu.edu

Abstract

Over the past two decades, several advances have been made in micromachined sensors and actuators. As the field of microelectromechanical systems (MEMS) has advanced, a clear need for the integration of materials other than silicon and its compounds into micromachined transducers has emerged. Piezoelectric materials are high energy density materials that scale very favorably upon miniaturization and that has led to an ever-growing interest in piezoelectric films for MEMS applications. At this time, piezoelectric aluminum-nitride-based film bulk acoustic resonators (FBAR) have already been successfully commercialized. Future innovations and improvements in inertial sensors for navigation, high-frequency crystal oscillators and filters for wireless applications, microactuators for RF applications, chip-scale chemical analysis systems and countless other applications hinge upon the successful miniaturization of components and integration of piezoelectrics and metals into these systems. In this article, a comprehensive review of micromachined piezoelectric transducer technology will be presented. Piezoelectric materials in bulk and thin film forms will be reviewed and fabrication techniques for the integration of these materials for microsensor applications will be presented. Recent advances in various piezoelectric microsensors will be presented through specific examples. This review will conclude with a critical assessment of the future trends and promise of this technology.

Keywords: piezoelectric MEMS, microsensors, lead zirconate titanate, aluminum nitride, zinc oxide, quartz, relaxor ferroelectrics, piezoelectric etching, accelerometers, gyroscopes, infrared detectors, FBARs, ultrasonic transducers, scaling laws for piezoelectric sensors, quartz crystal microbalance, viscoelastic properties of biomolecules

(Some figures in this article are in colour only in the electronic version)

1. Piezoelectric MEMS

Piezoelectric materials provide a direct transduction mechanism to convert signals from mechanical to electrical domains and vice versa. The reversible and linear piezoelectric effect manifests as the production of a charge (voltage) upon application of stress (direct effect) and/or as the production of strain (stress) upon application of an electric field (converse effect). Transducers using piezoelectric materials can be configured either as actuators, when the design of the device is optimized for generating strain or stress using the converse piezoelectric effect, or as sensors when the design of the device is optimized for the generation of an electric signal, using direct piezoelectric effect, in response to mechanical input. Typically, piezoelectric sensors are configured as direct mechanical transducers or as resonators, where the observed resonance frequency and amplitude are determined by the

---

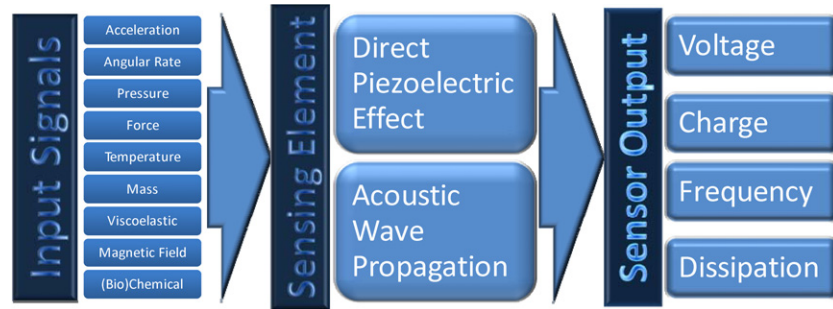[1] Author to whom any correspondence should be addressed.

Figure 1. Schematic illustration of the two modes of operation of piezoelectric sensors.

physical dimension properties and materials comprising the device and most importantly by mechanical and interfacial inputs to the device. Figure 1 schematically illustrates these configurations of piezoelectric sensors. Favorable scaling of piezoelectricity with miniaturization has led to a growing interest in piezoelectric films for microsystem applications.

However, most piezoelectric and ferroelectric materials are typically made out of nitrides and oxides of metals and semiconductors and tend to be relatively inert. Their deposition and crystallization processes typically involve high temperatures in the range 200–800 °C and these materials often include elements that are incompatible with standard CMOS technology. Furthermore, piezoelectric properties are critically dependent upon the stoichiometry and the morphology of these materials and therefore need appropriate seed layers and proper control of the nucleation, growth and crystallization processes of these materials. Despite these formidable challenges, recent advances in the development of low cost, high quality deposition processes of piezoelectric materials such as sputtering of aluminum nitride films, or chemical solution deposition of ferroelectric lead zirconate titanate (PZT) films and their patterning using plasma processes have made it possible to successfully integrate these materials into microsensors. The remainder of this review will outline the current challenges and opportunities in the successful implementation of micromachined piezoelectric sensors.

2. Miniaturization of piezoelectric sensors

There are essentially three approaches to realizing piezoelectric MEMS devices: (i) deposition of piezoelectric thin films on silicon substrates with appropriate insulating and conducting layers followed by surface or silicon bulk micromachining to realize the micromachined transducers ('additive approach'), (ii) direct bulk micromachining of single crystal or polycrystalline piezoelectrics and piezoceramics which are thereafter appropriately electroded to realize micromachined transducers ('subtractive approach') and (iii) integrate micromachined structures in silicon via bonding techniques onto bulk piezoelectric substrates ('integrative approach'). Depending upon the exact physical size of the desired mechanical sensors, each of these approaches offer specific advantages as illustrated schematically in figure 2.
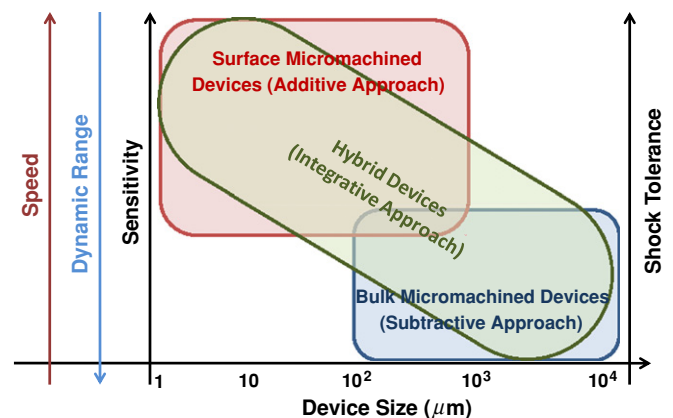

Figure 2. Three approaches toward fabricating piezoelectric MEMS devices.

We begin this section by a discussion on systematic approach toward designing a piezoelectric sensor.

By definition, the best sensors are designed to exchange minimal amount of energy with the measurand since this ensures minimal perturbation in measurements. From this perspective, it is beneficial to miniaturize sensors so long as the signal-to-noise ratio of the device can be maintained or improved upon miniaturization. Piezoelectric materials have very attractive electromechanical properties for realizing micromachined sensors and actuators [1–3]. The piezoelectric phenomenon is a reliable mechanism that does not exhibit failure modes associated with charge storage; it is reversible and typically linear. Piezoactuators, on the other hand, do not scale attractively upon miniaturization since the total amount of energy in small systems decreases with decrease in volume. However, since the natural resonance frequencies of micromechanical systems are typically high (kHz range), it is possible to obtain reasonable power from such miniaturized systems. Furthermore, micromachined piezoelectric actuators are capable of sub-microsecond response times and can be operated at low bias voltages (5–15 V) while consuming only microwatts of power.

The most successful piezoelectric MEMS devices at present are the commercially available aluminum-nitride-based film bulk acoustic resonators (FBARs) from Agilent Technologies [4]. Another commercially available piezoelectric MEMS sensor is the family of quartz gyroscopes from Systron Donner division of BEI Technologies [5].
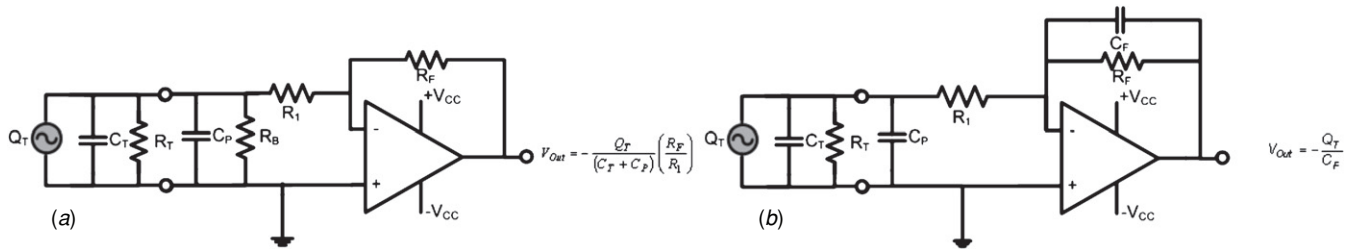
Figure 3. Typical circuits used with piezoelectric transducers. The sensor element is represented as a charge source Q_T with an equivalent capacitance C_T and leakage resistance R_T all connected in parallel. (*a*) Voltage amplifier circuit and (*b*) charge amplifier circuit.

MEMS devices using ZnO films have also been demonstrated [6]. Both ZnO and AlN materials are compatible with existing semiconductor fabrication lines [7]. However, these films exhibit small electromechanical coefficients that restrict their use primarily to acoustic resonator or sensing applications. In comparison, ferroelectric thin films such as $PbZr_{0.52}Ti_{0.48}O_3$ (PZT 52/48) and $PbMg_{1/3}Nb_{2/3}O_3$–$PbTiO_3$ (PMN–PT) have a clear advantage in actuator applications because they have piezoelectric $e_{31,f}$ coefficients 5–30 times higher than can be achieved in piezoelectric materials such as ZnO and AlN.

There are no universal scaling laws for piezoelectric sensors that can be applicable for all sensing quantities of interest. However, it can definitely be concluded that miniaturization is beneficial so long as the sensor is effective in interacting (coupling) with the measurand simply from the perspective that such sensors absorb very little energy in the process of measurement and therefore do not perturb the systems in the process of measurement. At the nanoscale, where it is conceivable that the material properties are not necessarily invariant with scaling, additional advantages and challenges from miniaturization can follow.

3. Signal conditioning circuits for piezoelectric sensors

A piezoelectric sensor can be modeled as a charge source Q_T with a shunt capacitor C_T and resistor R_T or as a voltage source with a series capacitor and resistor. The charge produced depends on the piezoelectric constant of the device and the input mechanical signals. The capacitance is determined by the area, the width and the dielectric constant of the piezoelectric material. The resistance accounts for the dissipation of static charge through leakage. Operational amplifier-based circuits can be readily used for amplification of piezoelectric sensors [8]. The voltage amplifier circuit shown in figure 3(*a*) is typically used when the amplifier circuit can be located very close to the transducer and when the effect of the parasitic capacitance C_P can be minimized in the performance of this circuit. The resistor R_B is typically very large and provides the required biasing for the input stage of the circuit. The charge amplifier circuit is based on the Miller integrator circuit as shown in figure 3(*b*). The feedback resistor R_F is required to prevent the circuit from saturating due to the charge build-up on the capacitor C_F. In this circuit, the amplifier keeps the two input terminals at the same voltage, and therefore the parasitic capacitance does not affect this circuit.

4. Review of piezoelectric materials for MEMS sensor and actuator applications

This section reviews prominent piezoelectric materials used in MEMS sensors and actuators from an applications perspective. Figures of merit (FOM) such as the piezoelectric coefficients, electromechanical coupling coefficient, mechanical quality factor and acoustic impedance of the selected materials will be used as metrics to determine the effectiveness of a given material for specific applications. Advantages and disadvantages of the integration and micromachining of materials will be discussed. Piezoelectric materials' history and properties in bulk form are available in numerous books [9–12]. Comprehensive piezoelectric thin film materials' and devices' reviews, which have seen much progress in the past 20 years, are also available to the interested reader [1–3, 13].

4.1. Piezoelectric materials' figures of merit

In any discussion of piezoelectricity the piezoelectric constitutive equations should be introduced, as in equations (1) and (2), where S_j is the mechanical strain, σ_j is the mechanical stress, E_i is the electric field, D_i is the electrical displacement, c_{ij} is the elastic stiffness constant, s_{ij} is the elastic compliance coefficient, and ε_{ii} is the permittivity. If a parameter has a superscript, such as s_{ij}^E, this is the elastic compliance when the electric field is held constant. The piezoelectric coefficients, d_{ij} and e_{ij}, are third rank tensors which in reduced tensor notation correspond to a 3 × 6 matrix. In this reduced notation, the indices ($i = 1$–3) define normal electric field or displacement orientation, ($j = 1$–3) define normal mechanical stresses or strains and ($j = 4$–6) represent shear strains or stresses:

$$D_i = d_{ij}\sigma_j + \varepsilon_{ii}^T E_i \quad \text{or} \quad D_i = e_{ij}S_j + \varepsilon_{ii}^S E_i \quad (1)$$

$$S_j = s_{ij}^E \sigma_j + d_{ij}E_i \quad \text{or} \quad T_j = c_{ij}^E S_j - e_{ij}E_i. \quad (2)$$

These equations are useful in describing the basic relationships for the direct and converse piezoelectric effects. In the direct effect using equation (1), a mechanical stress σ_j or strain S_j causes a net electrical displacement, D_i, on the i faces of the material, the magnitude of which depends on d_{ij} and e_{ij} respectively. Similarly, the converse effect expressed by equation (2) relates the induced normal and shear stress or strain to the applied electric field via the piezoelectric coefficient tensor [10]. In general, large d

piezoelectric coefficients, with units pC N^{-1}, are desired in actuator applications and large e coefficients are desired for sensor applications [14].

An effective d_{ij} and e_{ij} coefficient must be calculated to compensate for the clamping piezoelectric thin films experience in a composite structure, usually in between electrode layers on a Si substrate. Until recently, the effective d_{33} coefficient that could be achieved in piezoelectric thin films was approximately half of the bulk counterpart [1]. However, recent advances in templated and textured growth of piezoelectric thin films have enabled achievement of piezoelectric coefficients in thin films that approach the values of their bulk counterparts [15, 16]. The subscript f, in equations (3) and (4), is added to note that this is not the intrinsic property of the piezoelectric material, but it includes properties of the substrate; the effective thin film piezoelectric coefficients can be calculated as [1, 3]

$$d_{33,f} = d_{33} - \frac{2s_{13}^E}{s_{11}^E + s_{12}^E} d_{31} \qquad (3)$$

$$e_{31,f} = e_{31} - \frac{c_{13}^E}{c_{33}^E} e_{33}. \qquad (4)$$

The electromechanical coupling coefficient is another important figure of merit in piezoelectric materials. Many definitions of the electromechanical coupling coefficient exist, each having its own special feature, but all are closely connected, as outlined by Ikeda [9]. The expression that will be used in this review is

$$k_{33}^2 = \frac{d_{33}^2}{\varepsilon_{33}^T S_{33}^E}. \qquad (5)$$

The coupling coefficient is the square root of equation (5) and represents the ratio of the mechanical (electrical) energy converted to the input electrical (mechanical) energy for the piezoelectric material [10]. The orientation of the coupling coefficient is important, and must be distinguished clearly. The planar coupling coefficient, k_p, describes the radial coupling in a thin disc, when the electrical field is applied through the thickness, and the thickness coupling coefficient, k_t, is identical to k_{33} when the element is clamped laterally [17]. Mechanical quality factor describes the ratio of strain in phase with the stress to the strain out of phase with the stress in the vibrating body [17]. It can characterize the sharpness of the electromechanical resonance spectrum, which is very important in resonators [14].

4.2. Deposition, growth and properties of piezoelectric materials

Piezoelectric materials can be available in bulk or thin film forms for sensor applications. These materials in either form can be integrated using appropriate micromachining techniques into micromechanical structures to realize sensitive sensors. Critical to the realization of a piezoelectric micromachined transducer is the deposition of the piezoelectric material in the form of thin films from 1/10th of a micron to several tens of microns in thickness with piezoelectric properties approaching those of the corresponding bulk materials. Properties of thin film
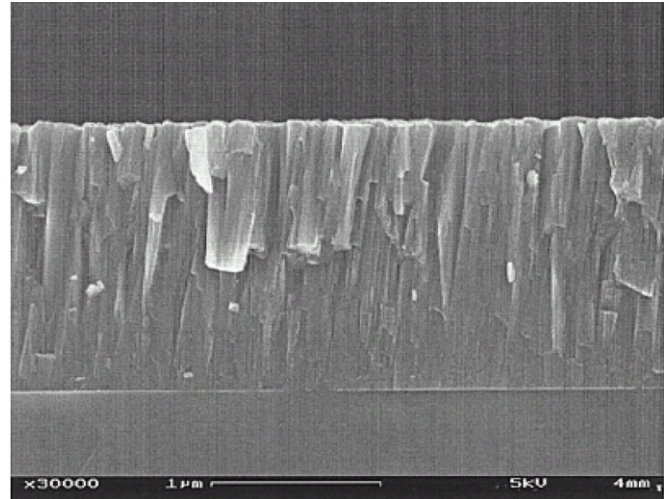

Figure 4. Cross-section of a sputtered AlN thin film observed using a transmission electron microscope clearly shows the columnar growth with the c-axis oriented perpendicular to the plane of the substrate [18].

piezoelectric materials depend upon (i) stoichiometry, (ii) film morphology, (iii) film density, (iv) impurities and (v) defects. In order to obtain a large response to mechanical deformations, piezoelectric films have to be grown with a textured structure with a high degree of alignment of the piezoelectric (poling) axis. In addition to the conditions used for the growth process, the orientation and quality of the substrate material is also found to have a strong influence on the nucleation and subsequent growth of the piezoelectric films. For these reasons, piezoelectric films are typically grown over an appropriate seed layer, for example (1 1 1) Pt. Figure 4 shows a typical SEM of the columnar structure obtained in a sputter-deposited piezoelectric film.

Piezoelectric thin films can be deposited by several techniques such as sputtering, chemical solution methods, screen printing and atomic layer deposition technique. Typically, all these methods involve three main steps: (i) generation of atomic or molecular species of interest, (ii) transport and condensation (deposition) of these on the substrate and (iii) post-deposition crystallization and annealing of the film. Furthermore, depending upon how the atomic or molecular species are generated and brought onto the substrate, the methods can be broadly classified into chemical methods (e.g. chemical vapor deposition, sol–gel techniques, etc or physical methods (e.g. sputtering, molecular beam epitaxy, pulsed laser deposition, etc. For each of the piezoelectric material of interest, several of these methods have been explored with varying degrees of success and advantages. The details of the techniques and the issues relating to the deposition and quality control of the films are too large for this short review; however, several excellent articles are available [1–3, 13, 19]. Table 1 summarizes most important techniques and the typical properties of the piezoelectric thin films currently in use or of interest in MEMS devices. Important piezoelectric materials and the current state of the art in their integration in micromachined transducers is briefly discussed next.

Table 1. Summary of the important techniques and typical properties of the piezoelectric thin films currently in use in MEMS.

Material	Deposition method	Deposition rate/film thickness	Substrate temp. (°C)	Reported piezoelectric properties
AlN/z–LiNbO$_3$ [26]	dc magnetron sputtering	6 nm min^{-1}	200	$k = 0.14$–0.17
AlN/Pt(1 1 1) [19]	Pulsed dc magnetron sputtering	0.4 μm	400	$e_{31,f} = 1.0$ pC m^{-2}, $d_{33,f} = 3.4$ pC N^{-1}, $\tan(\delta) = 0.002$, $k = 0.23$
AlN [27]	Reactive sputtering	1 μm	300	$e_{31,f} = -0.58$ pC m^{-2}, $d_{33,f} = 3.56$ pC N^{-1}, $k = 0.25$
AlN/Si(1 1 1) [28]	Metal organic chemical vapor deposition	130–250 nm	1050–1190	$d_{33} = 5.47$–6.56 pm V^{-1}
AlN/Si(1 1 1) [29]	Pulsed laser deposition	43–18 nm min^{-1}	500–920	–
ZnO/Pt [30]	Sol–gel	–	650, 700	$d_{33} = 17,11$ pm V^{-1}
ZnO/glass (Corning 7059) [31]	RF magnetron sputtering	18 nm min^{-1}	200	$k = 0.25$–0.26
ZnO/Si(0 0 1) [32]	RF magnetron sputtering	22 nm min^{-1}	Room temperature	–
ZnO/glass [33]	Pulsed laser deposition	45.8 nm	250	–
PZT/Pt(1 1 1)/Ti/ SiO$_2$/Si [34]	Chemical solution method	0.25–6 μm	700 (Sinter)	$e_{31,f} \simeq -7$ pC m^{-2}, $d_{33,f} = 150$ pC N^{-1}, $\tan(\delta) = 0.05$–0.02
PZT/LSMO/Si [35]	Hybrid powder sol–gel	~5 μm	800 (Sinter)	$d_{33,f} = 340$ pC N^{-1}, $\tan(\delta) = 0.02$
PZT/Si/SiO$_2$/Ti/ TiO$_2$/Pt [36]	Diol-based chemical solution deposition	4.1 μm	–	$e_{31,f} = 7.29$ pC m^{-2}, $\tan(\delta) = 0.023$
PZT/Ti/SiO$_2$/ Si(1 0 0) [37]	Pulsed laser deposition	1–3 μm	700	–

Quartz. Although found naturally, most quartz in practical use is synthetic, *AT*-cut single crystal, right handed and α-phase. Below the Curie temperature of 573 °C, quartz has a trigonal structure and above which it becomes β-quartz with a hexagonal structure [20]. Although the *AT*-cut is used for its near zero temperature coefficient of frequency, other cuts such as the *Y*-cut or the dual mode SC-cuts with high sensitivity of the resonance frequency with respect to temperature can be used accurate for temperature measurement [21]. Quartz is only useful in single crystal form and to achieve high resonance frequencies, the thickness of these crystal quartz must be minimized. Using micromachining technique resonators of thicknesses less than 10 μm and diameters less than 100 μm has been realized for quartz crystal microbalance applications and chemical sensing [22, 23]. Very few reports of epitaxial growth of quartz thin films exist in literature [24] and so quartz-based sensors are entirely based on bulk micromachining of quartz substrates.

Langasite. Another material that has similar temperature coefficients as quartz but a quality factor five times higher and three times higher piezoelectric coupling coefficient is Langasite, (La$_3$Ga$_5$SiO$_{14}$,) [25]. A relatively new non-ferroelectric piezoelectric material, langasite single crystals have been grown using the Czochralski method, and single crystal thin films have been grown using the liquid phase epitaxy technique [25]. Langasite does not experience phase transitions up to the melting point and has low acoustic wave propagation losses [25].

Lithium niobate and tantalate. Lithium niobate and lithium tantalate are well-known ferroelectric crystals discovered in 1949 and have been successfully grown into single crystals from melt by the Czochralski technique since 1965 [11]. Both are important in surface acoustic wave (SAW) devices and high-frequency filter applications. Like quartz, these materials must be grown in bulk and have different properties based on their cuts. The cuts usually used are *Y*-cut for LiNbO$_3$ and *X*-cut for LiTaO$_3$.

In summary, all of these materials namely quartz, langasite, lithium niobate and lithium tantalate are only available as bulk single crystals and currently no effective processes for their deposition in single crystal thin film form exist. These materials can be integrated in micromachined transducers only through direct bulk micromachining or hybrid integration methods. Table 2 lists the various material and piezoelectric properties of their bulk single crystal forms.

Zinc oxide and aluminum nitride. Both ZnO and AlN are piezoelectric materials with a wurtzite crystal structure [38]. Although the piezoelectric coefficients are up to nine times smaller than PZT, zinc oxide and aluminum nitride thin films have been used for bulk acoustic wave (BAW) applications [39, 40]. Unlike ferroelectric materials, the polar axis of these materials cannot be oriented by the application of electric field. Therefore, development of any deposition process for these films has to result in films with a well-oriented *c*-axis. Initial reports of integrating piezoelectric materials in micromachined sensor structures [6] were mainly based upon zinc oxide since these films are easy to produce at room temperature by reactive sputtering of zinc in oxygen environment followed by a high temperature anneal [31, 32, 41]. However, ZnO being a semiconductor with a bandgap of ~3 eV tends to be lossy with relatively smaller breakdown voltages. Any inadvertent doping of the material during deposition further exacerbates this problem. Recently, high quality AlN films have been developed as a good alternative to ZnO films [19, 26, 28]. Aluminum nitride has a much larger bandgap of 6.1 eV and there has been a considerable interest in

Table 2. Mechanical and electromechanical properties of piezoelectric quartz, langasite crystal, lithium niobate and lithium tantalate.

Property	Units	α-quartz (*AT*-cut)	La$_3$Ga$_5$SiO$_{14}$	LiNbO$_3$ (*Y*-cut)	LiTaO$_3$ (*X*-cut)
Density	g cm^{-3}	2.65 [11]	5.754 [43]	–	–
k	%	$k_p^2 = 8.8$–14 [11]	$k_p^2 = 15$ [44]	$k_{15} = 68$ [9]	$k_{15} = 43$ [9]
				$k_{31} = 17$ [9]	$k_{31} = 19$ [9]
				$k_{33} = 3$ [9]	$k_{33} = 5$ [9]
				$k_t = 16$ [9]	$k_t = 18$ [9]
Q_m		10^4–10^6 [17]	15 000 [44]	10^5 [11]	10^5 [11]
d	pC N^{-1}	$d_{11} = -4.6$ to 2.3 [11]	–	–	–
		$d_{14} = -0.67$ [20]			
e	C m^{-2}	$e_{11} = 0.173$ [20]	$e_{11} = -0.45$ [43]	$e_{15} = 3.7$ [9]	$e_{15} = 2.6$ [9]
		$e_{14} = 0.04$ [20]	$e_{14} = 0.077$ [44]	$e_{22} = 2.5$ [9]	$e_{22} = 1.86$ [45]
				$e_{31} = 0.3$ [45]	$e_{31} = -0.22$ [45]
				$e_{33} = 1.77$ [45]	$e_{33} = 1.9$ [9]
$\varepsilon_{11}^T/\varepsilon_0$		4.6 [11]	18.99 [46]	84 [9]	51 [9]
$\varepsilon_{33}^T/\varepsilon_0$		4.6 [11]	49.32 [46]	30 [9]	45 [9]
TCF[a]	ppm °C^{-1}	$\sim$0 [11]	1.6 [44]	69 [47]	-40 [48]
T_c	°C	–	–	1210 [9]	660 [9]

[a] TCF: temperature coefficient of frequency.

Table 3. Comparison of the mechanical and electromechanical properties of zinc oxide, aluminum nitride and PZT materials.

Property	Units	AlN	ZnO	PZT (thin film, 1–3 μm)
Density	g cm^{-3}	3.26 [11]	5.68 [11]	7.5–7.6 [11]
k_t^2	%	6.5 [43]	9 [43]	7–15 [49]
Q_m @ 2 GHz		2490 [43]	1770 [43]	
$k_t^2 Q_m$ @ 2 GHz		160 [38]	160 [38]	
$e_{31,f}$	C m^{-2}	-1.05 [43]	-1.0 [43]	-8 to 12 [49]
$d_{33,f}$	pm V^{-1}	3.9 [43]	5.9 [43]	60–130 [49]

III-nitride materials due to their excellent photonic properties and possibility of bandgap engineering [42]. Textured columnar growth thin films of AlN with the *c*-axis oriented perpendicular to the substrate have been successfully sputter deposited in the 200–500 °C temperature range. The low loss values of tan(δ) $\sim$ 0.001 and good electromechanical coupling coefficient of $\sim$0.25 achieved in thin film form have made is possible to realize high *Q*-factor BAW resonators from aluminum nitride. Table 3 lists the typical piezoelectric properties of AlN, ZnO and PZT thin films.

Lead zirconate titanate. In thin film form, PZT films are the most widely used ferroelectric materials [50]. The higher electromechanical coefficient of PZT films makes it a very attractive material for microactuator and microsensor applications [1, 2, 13]. A variety of growth methods have been used to deposit PZT thin films including sputtering [51], sol–gel [52], MOCVD [4] and laser ablation processes [53]. The sol–gel process enables uniform deposition of high quality films with well-controlled compositions on large diameter substrates at low cost [52, 54]. PZT films at the morphotropic phase boundary with a Zr/Ti ratio of 52/48 have been shown

to exhibit a maximum in the piezoelectric response and are typically used in MEMS device applications. For fabrication of thicknesses between 1 and 100 μm, many thick film deposition techniques of PZT have been used such as screen printing, composite sol–gel, electrophoretic deposition, thick film sol–gel, direct writing and ceramic paint as Dorey and Whatmore outlined in [55]. Thick film techniques require very high temperatures (600–1200 °C) which can raise concerns with high diffusion speeds of atomic species. The preparation of PZT chemical solution formation and subsequent deposition of PZT 52/48 films onto substrate are described in detail in [56, 57].

Relaxor ferroelectrics. Lead-titanate-relaxor-based ferroelectric single crystal systems, PZN–PT, PMN–PT and PYN–PT, show extremely large electromechanical coupling coefficients and piezoelectric coefficients compared to PZT, but have integration issues that have limited their use in thin films such as high growth temperatures, lower dielectric constant and low stress response [38, 57]. The low Curie temperatures of PMN–PT and PZN–PT limit their operating range, where as PYN–PT has a higher Curie temperature. Research in relaxor ferroelectrics is still very promising due to the wide array of different compositions of the PbZrO$_3$–PbTiO$_3$–Pb(B$_1$B$_2$)O$_3$ ternary system. A comprehensive review of relaxor type ferroelectric materials is given in [58] and a comparison of the material properties is summarized in table 4.

4.3. Etching piezoelectric materials

Wet etching. In order to fabricate micromachined devices out of piezoelectric materials, it is necessary to selectively pattern them. The traditional method of patterning piezoelectric materials involves reacting the material in a wet chemical (etchant) whereby the piezoelectric material reacts with the liquid etchant forming a water or solvent soluble product.

Table 4. Comparison of the lead-titanate-based relaxor ferroelectric materials and ferroelectric PZT.

Property	Units	PZT (bulk)	PMN-PT	PZN-PT	PYN-PT
Density	g cm^{-3}	7.5–7.6 [11]	7.6–7.8 [11]	8.31 [59]	
k_p^2	%	25–65 [11]	30–76 [11]		
d_{31}	pC N^{-1}	−27 to 274 [11]	−1330 [59]	−1154 [59]	500 [59]
d_{33}	pC N^{-1}	71–590 [11]	2820 [59]	2000 [59]	2500 [59]
Q_m		65–1200 [11]	43–2050 [11]		
T_c	°C	180–350 [11]	<150 [60]	<150 [60]	350 [60]

Table 5. Summary of the wet etching rates of various piezoelectric materials.

Material	Etchant	Temperature (°C)	Etch rate (μm min^{-1})	Comments
Quartz [62, 63]	NH$_4$F:HF	25	1.35 (*AT*-cut)	Use of BOE results in extremely polished etching of quartz. Good temperature control is necessary
AlN (epitaxial/bulk) [69, 77]	KOH	20	2.26	Does not etch in acids. Depending upon annealing temperature can be etched even in a weak base such as photoresist developer AZ400K
AlN (sputtered) [65, 66, 77]	H$_3$PO$_4$	60		
ZnO [7, 71]	HCl (1%)	20	10	Almost all acids etch ZnO extremely fast. Dilute acids need to be used for best control
ZnO (sputtered) [78]	HF (0.05 wt%)	20		
ZnO [7]	H$_3$PO$_4$ + CH$_3$COOH + H$_2$O	20	0.8	
PZT (bulk) [79]	Various acids	42–50		PZT can be etched in strong acids such as HCl, HNO$_3$, HF as well as bases such as KOH and NaOH. HCl tends to attack PZT along the grain boundaries whereas HF etches leave a whitish residue
PZT (sol–gel) [73]	(10NH$_4$F:1HF) + (2HCl:1H$_2$O)	23 and 42	0.13	
PZT (sol–gel) [74]	HCl:BHF:NH$_4$Cl:H$_2$O	20	0.96	

In this way, the exposed regions of the piezoelectric are clearly removed and pattern definition is achieved by the use of photolithography techniques. Unfortunately, most piezoceramic materials are characterized by excellent chemical stability making them very difficult to react in weak acid/base chemical solutions. However, most well-known piezoelectric materials can be wet etched in strong acids and bases. For example, quartz crystals are found to rapidly dissolve in NaOH and KOH solutions [61]. However, the most common polish wet etching method applicable to quartz is based on the use of NH$_4$F:HF solutions [62, 63]. Typically, the rates depend upon the crystallographic directions and therefore tend to be anisotropic in nature. A simple method for constructing the expected etch profile in NH$_4$F:HF etching solution for quartz crystals is described by Danel and Delapierre [64]. Aluminum nitride can be wet etched in hot phosphoric acid between 60 and 95 °C [65–67]. The etch rate itself varies depending upon the quality of the aluminum nitride formed. For sputter-deposited and annealed stoichiometric/epitaxial AlN films, the etch rate can be as low as 14 nm min^{-1} whereas highly defective AlN:H films could be etched orders of magnitude faster in 85 °C hot phosphoric acid [67]. Similar observations were also reported in KOH-based etching solutions for aluminum nitride [68, 69]. The advantage of using the AZ400K

(KOH-based) developers is that the process is compatible with photolithographic processes and does not attack the photoresist. Zinc oxide on the other hand is readily soluble in most single acids, mixed acids, alkaline solutions and ammonium chloride [70]. Extremely fast, reaction-rate-limited ZnO etch rates in HNO$_3$:HCl:H$_2$O solutions have been reported by Li *et al* [71] whereas much more controlled etch rates were obtained using H$_3$PO$_4$:CH$_3$COOH:H$_2$O solutions [7]. The advantage of the latter etch process is that it does not attack aluminum which is often used as the electrode materials in ZnO-based devices. PZT substrates are also attacked by strong acids and alkaline solutions [72]. It was also observed that HCl-based etches rapidly dissolved PZT films and ceramics along the grain boundaries thereby rendering such processes unsuitable for fine feature patterning [73]. Zheng *et al* reported a BHF:HCl:NH$_4$Cl:H$_2$O-based etch process that is compatible with photolithographic processes [74]. The addition of NH$_4$Cl in this case is reported to form [PbCl$_4$]$^{2-}$ improving the dissolution rate of Pb and furthermore dilutes BHF and prevents photoresist attack. However, typical of all HF-based PZT etches, a white residue consisting of water-insoluble PbClF was obtained. This was removed by a short exposure to HNO$_3$:H$_2$O dip [74]. A similar two-step lithographically compatible etch process was developed by Wang *et al* [73]. They used a 10NH$_4$F:1HF BOE etchant

followed by 2HCl:1H$_2$O dip to remove the white lead fluoride residue. Table 5 summarizes the wet etching characteristics of various piezoelectric materials.

Wet etching techniques, while relatively simple, can both detrimentally affect the piezoelectric properties and are often incompatible with other films used as part of the device structure [75].

Dry etching. Dry etching techniques based upon the use of reactive plasma offer very attractive alternatives to the wet patterning techniques for piezoelectrics. Pioneering work in identifying the role of ions in reactive plasma etching was done by Steinbruchel [76]. Since then, several gas species have been used for etching of the various piezoelectric materials. The main consideration in the choice of gas species for plasma etching depends upon the formation of volatile products as part of the breakdown of the metal (semiconductor) oxides being etched.

Most piezoelectric materials are primarily etched via physical sputtering with the chemical species assisting the process. The role of the chemical species is clearly observed in the comparative etching experiments of SiO$_2$ (quartz) and lithium niobate/tantalate [80]. In these experiments, it is clearly observed that increasing the ratio of CF$_4$ to CHF$_3$ has no effect on the etch rate of lithium niobate/tantalate whereas it significantly increased the etch rate of SiO$_2$ where a regime of ion-enhanced chemical etching is obtained. Since the fluorides of lithium and tantalum oxide and niobium oxide are all non-volatile, the reactive component of etching is an insignificant part of the etching process, which simply relies on the physical sputtering of the surface atoms due to the bombardment of energetic ions. Therefore, most piezoelectric etching recipes use inert gases as part of the etch gas composition as the sputter yield of inert gases is much higher than other elements/molecules [81]. Quartz substrates have been etched with very high aspect ratios and very high surface smoothness using SF$_6$ and Ar/Xe gases [82, 83]. The use of heavier Xe helps reduce the redeposition and more effectively removes any non-volatile residues resulting in smoother surfaces with an average surface roughness of ~2 nm. Aluminum nitride is typically etched using chlorine chemistries since aluminum fluoride is an extremely stable and non-volatile compound [84, 85]. Shul *et al* have studied the comparative etching of GaN, InN and AlN in chlorine and BCl$_3$ plasmas and were able to achieve etch rates of 0.23 μm min^{-1} for AlN in BCl$_3$ plasma with a small percentage addition of Ar/N$_2$ [86]. The etching characteristics of ZnO and etch selectivities of ZnO to SiO$_2$ in CF$_4$/Ar, Cl$_2$/Ar and BCl$_3$/Ar plasmas are reported by Woo *et al* [87]. High etch rates of 0.12 μm min^{-1} have been reported. In several of the reported optimization of the etch processes, it is important to ensure that the photoresist mask is able to survive the piezoelectric material patterning. Often, such optimization compromises the etch rate of the material since such etches are performed under high pressure and low substrate bias conditions. In cases where it is necessary to use a hard mask, typically electroplated nickel is used. Nickel has been reported to provide a very high selectivity in fluorine plasmas > 30:1
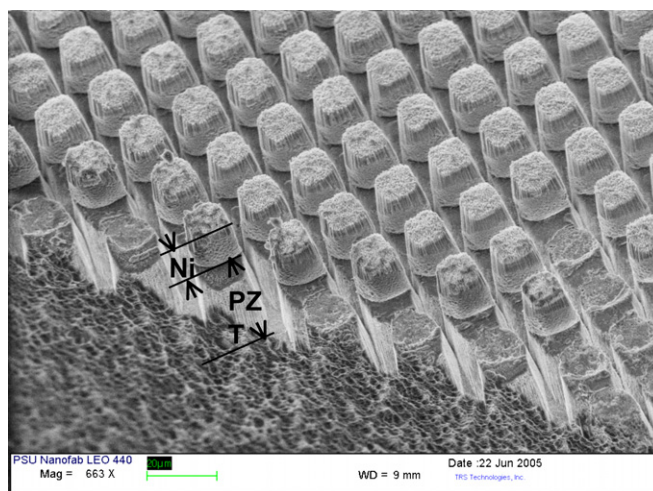

Figure 5. SEM image of the etched feature in the PZT ceramic substrate with a minimum feature size of 3 μm. Almost vertical sidewalls were obtained.

for PZT etching [88]. PZT is typically etched in fluorine or chlorine plasma. Using SF$_6$ and Ar, several groups have reported high aspect ratio etching of PZT. In our work on PZT etching, a maximum etch rate of 19 μm h^{-1} for PZT-4 and 25 μm h^{-1} for PZT-5A compositions has been obtained using fluorine-based plasma chemistry [83]. We have also demonstrated a high aspect ratio etch (>5:1) on a 3 μm feature size. Figure 5 shows the SEM image of the etched features for PZT. The square pillars created have a lateral dimension of 15 μm with a gap of 3 μm in between. The etched depth was ~15 μm. Almost vertical sidewalls with relatively smooth surfaces were obtained. 2–5 μm thick nickel on Cr/Au was used as the hard mask. A selectivity of ~25 between the nickel hard mask and PZT was obtained. The availability of reliable, high throughput, high aspect ratio micromachining processes has now created new opportunities for realizing novel MEMS devices from bulk piezoelectric materials such as quartz, lithium tantalate, aluminum nitride, PZT and single crystal PMN-PT. Table 6 summarizes the dry etching of various piezoelectric materials.

5. Integration of piezoelectric materials into micromachined structures

5.1. Bulk micromachining piezoelectrics (subtractive approach)

Bulk micromachining of piezoelectric materials is of considerable interest since it allows for the direct integration of sensors and actuators into a single structure. Additionally, the optimized and often superior properties of bulk materials can be directly harnessed for these applications. However, high aspect ratio etching of piezoceramic materials is inherently challenging since most of these complex oxide materials are very stable and are not readily amenable to selective chemical reactions necessary for patterning. However, inductively coupled reactive ion etching (ICP-RIE) can be used to produce structures with vertical sidewalls and flat faces.

Table 6. Summary of the dry etching characteristics of various piezoelectric materials.

Material	Etch gas(es)	Pressure (Torr)	RF frequency (MHz)/power (W)	Etch rate (μm min^{-1})	Comments
Quartz [89]	CF_4	2.7	27 MHz	4	Non-lithographic plasma confinement method was used
Quartz [82]	SF_6/Xe	0.0045	13.56/90	0.4	ICP source with 150 W power was used to obtain a highly smooth surface
Pyrex 7740/quartz [90]	SF_6/Ar	0.002	13.56/475	0.54	ICP source with 2 kW power was used. Highly smooth surface with $R_a = 1.97$ nm. Similar rates were obtained for quartz etching as well
$LiNbO_3$/$LiTaO_3$ [80]	CHF_3/CF_4	0.05	13.56/350	~0.01	Etching proceeds mainly via physical sputtering
AlN [91]	Cl_2/Ar	0.005	13.56	0.75	ICP source with 500 W power was used. Etching proceeds by physical bombardment. No significant etching was observed below a threshold substrate voltage of -50 V. The paper also reports etching GaN and AlGaN. Another good reference is [86]
AlN [84]	BCl_3/Cl_2/Ar	0.005	13.56	>0.4	
ZnO [92]	$SiCl_4$/Ar	0.175	13.56/0.56 W m^{-2}	0.027	Additional references on ZnO etching are available [87, 93]. Typically etching is found to proceed via physical bombardment
ZnO [94]	C_2H_6/H_2/Ar	0.005	13.56/300	0.05	
PZT (Bulk) [88]	SF_6	0.005	13.56/200	0.12	In [88], pure SF6 gave the best etch rate but the angle was shallow which could be improved by Ar addition but at the cost of etch rate. The recipe used in [83] mainly uses physical sputtering; however, aspect ratios of >5:1 were obtained
PZT [95]	CF_4/80% Ar	0.015	13.56/700	0.143	
PZT [83]	SF_6:Ar::1:10	0.005	13.56/475	0.42	

Using multiple front and backside masks, ICP-RIE etches at various depths can produce stair-stepped structures from bulk piezoelectric materials typically 100 μm thick substrates. Masked metallization provides ground and power electrodes that activate and/or measure the charge-developed specific areas in the structure to enable truly revolutionary MEMS devices.

However, piezoelectric transducers realized using bulk micromachining processes have been limited due to the lack of reliable and fast etching processes. Notwithstanding this, some reports of bulk micromachined sensors and actuators, based upon some of the etching processes described, can be found in the literature. Bulk micromachined quartz resonator arrays for gravimetric biochemical sensing applications have been reported by several groups [96–101]. These will be discussed in greater detail in the following section. Piezoelectric micromachined ultrasonic transducer (pMUT) is another device which has been realized by direct micromachining of piezoelectric materials. Jiang *et al* [102–104] have reported the performance of diced and micromachined single crystal PMN-PT/epoxy composites with center frequencies in the 5–40 MHz range. The measured electromechanical coefficients for composites with frequencies of 5 MHz–15 MHz were about 0.78–0.83, and the coupling coefficients for composites with frequencies of

Figure 6. SEM picture of etched PMN–PT posts for piezoelectric composite micromachined ultrasonic transducer (PC-MUT) composites. The micro-posts are about 8 μm wide and >40 μm long [104].

25 MHz–40 MHz were about 0.71–0.72. Figure 6 shows an SEM picture of an array of etched PMN–PT pillars forming PC-MUT prior to filling with polymer and the deposition of the top gold electrode.

More recently, we have reported on the fabrication and performance of a bulk micromachined PZT actuator [105]. Figure 7 shows the photograph of a bulk micromachined PZT
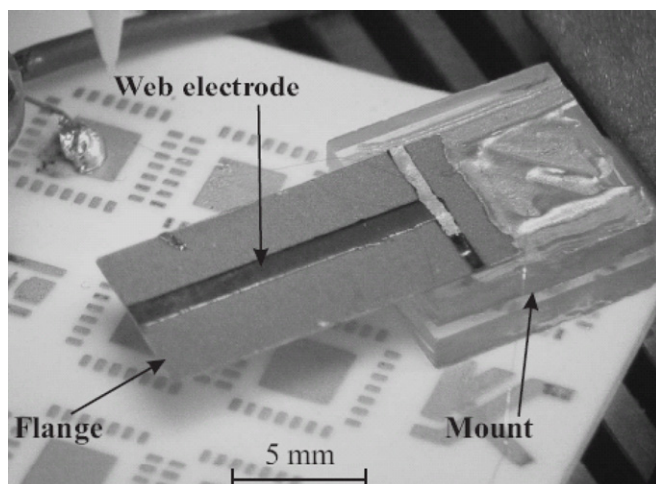
Figure 7. Photograph of the fabricated T-beam actuator. The flange is 83 μm thick whereas the web region is 100 μm thick.
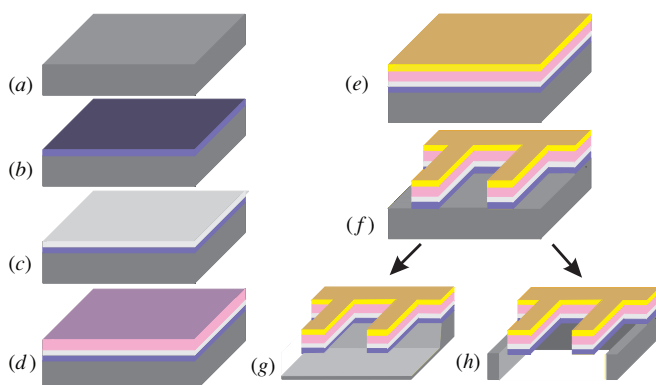

Figure 8. Schematic illustration of the surface micromachining process. (*a*) Substrate silicon wafer; (*b*) silicon substrate surface is thermally oxidized; (*c*) bottom electrode such as a (1 1 1) platinum film is deposited; (*d*) the piezoelectric thin film is deposited and annealed; (*e*) top electrode metal such as Cr/Au is deposited; (*f*) the entire piezoelectric, electrodes and passive layer stack is patterned and etch to expose the substrate silicon; (*g*) substrate silicon is etched from the front side using anisotropic wet etchant or isotropic vapor phase XeF$_2$ etchant while protecting the transducer stack and (*h*) alternatively, the substrate silicon is anisotropically etched from backside to release the transducer structure.

T-beam actuator. Finely polished, 100 μm thick PZT-4 with Cr/Au electrode was patterned and etched 17 μm using an ICP-RIE process with a nickel hardmask. The etch process used 50 sccm Ar and 5 sccm SF$_6$ at 2000 W ICP power and 475 W substrate power at an etch rate of 19–25 μm h^{-1} [83].

5.2. Surface micromachining (additive approach)

5.2.1. A typical piezoelectric transducer stack and patterning.
A typical surface micromachining process begins with the sequential deposition of passive, active and electrode layers in the order desired. The piezoelectric device stack is patterned using wet or dry micromachining processes. Finally, the exposed sacrificial layer is etched to release the freestanding piezoelectric sensor structure. Figure 8 schematically illustrates the surface micromachining process.

The complete piezoelectric sensor stack with patterned electrodes is realized by various etching techniques. In any given sensor configuration, the stack consists of electrodes, piezoelectric films, passive support materials and the substrate. (1 0 0) Silicon is the typical substrate material in MEMS devices. Layer(s) of silicon dioxide, silicon nitride and polysilicon of varying thickness are further deposited on such a substrate and in the order desired to form the required sensor passive and sacrificial layers. These films are typically deposited using low pressure chemical vapor deposition in silane, ammonia, nitrous oxide environment, and further references for the growth and the mechanical properties of these films can be found in [106, 107]. Electrode films are typically deposited using sputtering and vacuum evaporation techniques.

Using a combination of sputtering, chemical solution deposition, evaporation, etc, the piezoelectric thin film sensor stack is typically realized. Depending on the film orientation and placement of electrodes in the sensor configuration, either longitudinal or shear stress can be sensed with respect to the primary piezoelectric *c*-axis of the film. Normally, the piezoelectric film is sandwiched between two electrode layers or an interdigitated electrode pattern is placed on the top surface of the piezoelectric film for the measurement of the charge or voltage in the sensing structure. In the former case, the bottom electrode layer is used as the seed layer upon which textured piezoelectric films are deposited. In order to allow for uniform nucleation and high degree of structural orientation, the bottom electrode layer is therefore not patterned. Following the deposition of the piezoelectric film, the top electrode, typically gold or aluminum on a chrome adhesion layer, is deposited and lithographically patterned. Care must be taken that the chemicals used to develop the photoresist or the top electrodes do not react with the piezoelectric film or adversely affect their properties. The lift-off patterning technique can be used where compatible metal etchants cannot be found. Next, the sensor material stack consisting of the active and passive layers is etched through the piezoelectric material, the bottom electrode and the passive mechanical layers. The etching can be accomplished using wet chemical or plasma reactive ion etching techniques discussed in the previous section. High anisotropy achievable in high density plasma etching techniques provide more vertical and well-defined side walls, dimensional control and tolerance. Since the film thicknesses in surface micromachined sensors are only a few micrometers thick, these can be readily etched in the order of a few hours. Thick photoresists such as SPR 220 or AZ 4620 can be used for masking the stack during such etches. However, if the selectivity is not sufficient, photosensitive benzocyclobutene (BCB) such as Cyclotene® 4024 can be used as the photo patternable layer. If the etch process cannot be sufficiently optimized to provide sufficient selectivity to any of these polymer resist layers, patterned nickel hard masks can also be used for piezoelectric stack etching. The low sputtering rate and high inertness of nickel by-products in fluorine and chlorine plasmas provide sufficient selectivity for most applications. However, the use of such masks complicates the fabrication process considerably.
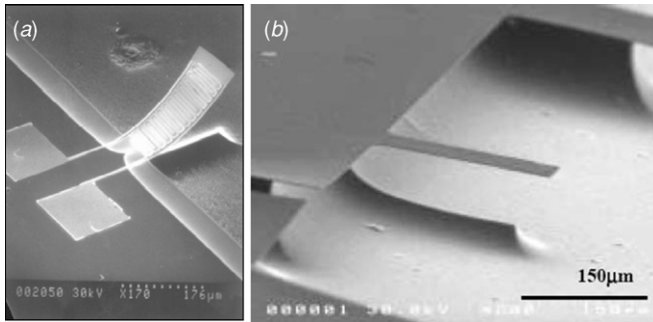
Figure 9. (*a*) Piezoelectric cantilever bending due to uncompensated stress in the fabricated structure and (*b*) stress-compensated cantilever structure based on a PZT bimorph structure [108].

Table 7. Typical layer thicknesses, residual stresses, and Young's modulus of materials in PZT transducer stack [111].

Film	Nominal thickness (Å)	Young's modulus (GPa)	Stress (MPa)
SiO$_2$	1000	60.2	33.1 ± 10
Si$_3$N$_4$	500	310 [112]	800 ± 200
SiO$_2$	3500	60.2	33.1 ± 10
Ti/TiO$_2$/	160/90/	141.4 (Pt value)	323 ± 83.3
Pt/TiO$_2$	1640/10		
PZT	5000	70.1	175 ± 7.26
Pt	1050	141.4	76.3 ± 16.5

5.2.2. Stress in piezoelectric thin films. As explained, typical surface micromachined piezoelectric transducers consist of several active and passive layers stacked together as part of the completed device. Successful design and fabrication of such transducers rely on a basic understanding of the built-in stress in the various layers used and its temporal evolution with exposure to environmental conditions. Failure to control these results in unbalanced stresses with large out-of-plane deflection of the released structures is shown in figure 9(*a*). Using the simplifying assumptions, such as one-dimensional stress along the length of the cantilever, no stress gradients within each of the layers of the films, and no external loading, a condition for zero curvature for discrete films, can be given by

$$\sum_{i=1}^{n} t_i \sigma_i h_i = \sum_{j=1}^{m} t_j \sigma_j h_j, \tag{6}$$

where t, σ and h are the thickness, residual stress and distance from the neutral plane respectively. The indices n and m represent the number of films above and below the neutral plane. The equation reveals an intuitive relationship; for zero deflection, the net force above and below the neutral plane must balance. In a systematic investigation performed by Gross [108], a series of micromachined cantilevers with varying PZT layer thickness on zirconia seed layer were fabricated and released. A near linear relationship between the PZT thickness and curvature of the cantilevers was observed where flat cantilevers were obtained for PZT thicknesses ∼300 nm for the stack of passive materials used in their work. Figure 9(*b*) shows a stress-compensated piezoelectric cantilever realized using a symmetric PZT–PZT bimorph layering.

In another set of experiments, Hong [57] studied the residual stress in thin film PZT layer on zirconia using the wafer flexure method on both thermally oxidized and plain silicon wafers. The apparent stresses of the zirconia and the first PZT layer were found to be significantly different from what is expected. It was observed that zirconia films on either Si or SiO$_2$/Si wafers exhibited stresses of 20–100 MPa after deposition. After an annealing process at 700 °C for 2 h, the stresses of the zirconia films became more compressive (to −40 MPa). This stress change is considered to arise due to the phase transformation from the tetragonal phase

to the monoclinic phase of the zirconia films which generates a volume expansion of 4% [109].

Aging effects were also observed in PZT actuator stacks on zirconia layers. It was observed that the exposure of the released PZT–zirconia cantilevers to elevated temperatures resulted in a change of their curvature. Brenier [110] observed that sol–gel zirconia films annealed at 400 °C were porous and adsorbed moisture during exposure to atmosphere and proposed the repulsion of the OH dipoles upon hydration of zirconium (Zr–OH species) as the cause for the observed compressive stress component. Table 7 summarizes the typical stress obtained in the various layers in a typical PZT–zirconia stack [111].

In the work on PZT RF switches by Polcawich, residual stress engineering was effectively used to create cantilever structures with negative curvatures [111]. This was achieved through the deposition of a dielectric multilayer film consisting of silicon dioxide and silicon nitride. The large tensile stress of the silicon nitride layer was coupled with the smaller tensile stress in the silicon dioxide layer to counter stresses within the electrode–PZT–electrode stack. In their design, the neutral axis of the composite stack was engineered to lie very close to the interface between dielectric composite and the base metal. This ensured positive deflection of the actuator upon d_{31} mode actuation while the residual stress gradient of the composite ensured a negative curvature under static equilibrium conditions. Figure 10 shows the residual stress-engineered PZT actuator structure.

5.2.3. Sacrificial layers and release etch. Depending upon the fabrication process used, the freestanding micromechanical sensing structure is released by either etching through the entire silicon substrate thickness in the desired regions or by undercutting the piezoelectric sensor stack using fast isotropic etching. For release of the sensor structure through bulk micromachining of the silicon substrate, double side alignment is typically required with the silicon etched from the opposing face from the piezoelectric stack. For through silicon wafer etch, anisotropic wet etchants such as potassium hydroxide (KOH), tetramethyl ammonium hydroxide (TMAH) and ethylene diamine pyrocatechol (EDP) can be used. Typically, these etches are performed in the temperature range of 60–100 °C and can take several hours to etch through a 500 μm thick silicon wafer. Often, these chemicals react with the piezoelectric thin films and adversely affect their properties. Therefore, it is necessary to protect the piezoelectric sensors
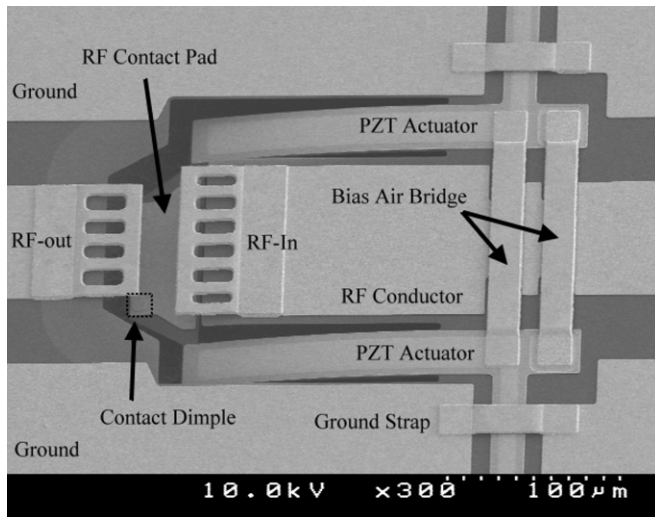
Figure 10. SEM picture of a PZT RF MEMS switch showing the residual-stress-engineered PZT actuator to result in a net negative curvature under unactuated conditions and allowing for a positive deflection upon d_{31}-mode actuation [111].

stack during etching from exposure to these chemicals. Deep reactive ion etching of silicon using a sequential process of etching and passivation provides a highly anisotropic through wafer etch capable of aspect ratios of 30:1. Such an etch is highly desirable since silicon dioxide and silicon nitride layers can be readily used as the etch stop layers. For release etches based on front side release of the sensor structure, 1–3 μm thick silicon dioxide and polysilicon layers are typically used. A silicon dioxide sacrificial layer is typically undercut in buffered HF. Once again, care must be taken to protect the piezoelectric films during such release since HF can attack the piezoelectric films. A more desirable release process is based on the sacrificial etching of polysilicon layer in vapor phase XeF$_2$ [113]. The etch is a purely chemical isotropic process and requires no other form of energy input for the etching to occur. XeF$_2$ has very high etch selectivity between silicon and all other known materials used in the semiconductor processes [114]. Etch rates greater than 1 μm min^{-1} have been reported which can be reduced by diluting XeF$_2$ with nitrogen.

5.3. Bonded piezoelectric devices (integrative approach)

An alternative approach is to integrate precision micromachined silicon structures on to PZT substrates. This has the advantage of being able to use the large array of silicon microfabrication techniques without the need to develop extensive micromachining capabilities for PZT. However, the success of this technique is predicated upon the availability of low-temperature (preferably <200 °C), precision aligned bonding techniques. A low temperature solder bonding technique such as those reported in [115–117] can be used to realize such micromachined transducers. As an example of a device realized using this technique, a bonded flextensional actuator on the PZT substrate has been recently reported [118]. Figure 11(a) shows the schematic diagram of

the micro flextensional actuator. It consists of a PZT substrate of length l_p, width w_p and a thickness t_p and poled through the thickness of the material. A beam of length l_b, width w_b and thickness t_b is micromachined in silicon and bonded at the two ends to the PZT substrate as shown. Using the d_{31} piezoelectric effect, a through-the-thickness electric field parallel to the poling direction results in a longitudinal PZT contraction and compressive stress in the silicon beam. The small PZT contraction is amplified by the clamped–clamped silicon micromachined structure as it moves transversely in response to the longitudinal compressive force. Depending on initial beam and/or bonding imperfections, the beam can either buckle up or down.

Figure 11(b) shows an optical photograph of the fabricated flextensional device using this technique and figure 11(c) shows the SEM picture of the freestanding silicon structure bonded onto the PZT substrate. In spite of successful demonstration of this technique, this method of fabricating piezoelectric MEMS devices has found limited use. Another example of a piezoelectric sensor based on the integrative approach is the earlier generation barium-strontium-titanate-based infrared detectors [119]. These will be discussed in greater detail in the following section.

6. Review of micromachined piezoelectric sensors

6.1. Piezoelectric bulk acoustic resonators

In wireless communications application, BAW resonators and filters have been gaining popularity over SAW technology due to improved insertion loss, temperature stability, power handling capability, electrostatic discharge (ESD) protection, selectivity and mechanical quality factor [4, 120]. The three most successful thin film, bulk acoustic resonators are the film bulk acoustic resonator (FBAR), solidly mounted resonator (SMR) and high overtone bulk acoustic resonator (HBAR).

Bulk acoustic wave resonators using piezoelectric materials can either be excited in thickness mode (TE) or with interdigitated electrodes providing lateral field excitation (LFE). In TE and LFE, the electric field is parallel and perpendicular to the direction of acoustic wave propagation, respectively. Typically, TE excites longitudinal waves with phase velocity $v_a = \sqrt{c_{11}/\rho}$ and LFE excites shear waves with phase velocity $v_a = \sqrt{c_{44}/\rho}$ for propagation along a crystal axis, where c_{ij} is the elastic stiffness constant and ρ is the density of the material. The governing impedance and admittance equations for TE and LFE resonators are

$$Z_{in} = \frac{1}{j\omega C_0}\left(1 - k_t^2 \frac{\tan(\theta/2)}{\theta/2}\right),$$
$$Y_{in} = j\omega C_0\left(1 + \kappa^2 \frac{\tan(\theta/2)}{\theta/2}\right), \tag{7}$$

respectively, where C_0 is the parallel plate capacitance of the resonator, $\kappa^2 = e^2/c\varepsilon$ is the piezoelectric coupling coefficient, $k_t^2 = \kappa^2/\kappa^2 + 1$, $\theta = \omega d/v_a$ and t is the thickness of the piezoelectric film. The resonator frequency response is characterized by alternating antiresonances (infinite impedance) at

$$\omega_a = \frac{N\pi v_a}{d}, \qquad N = 1, 3, 5, \ldots \tag{8}$$
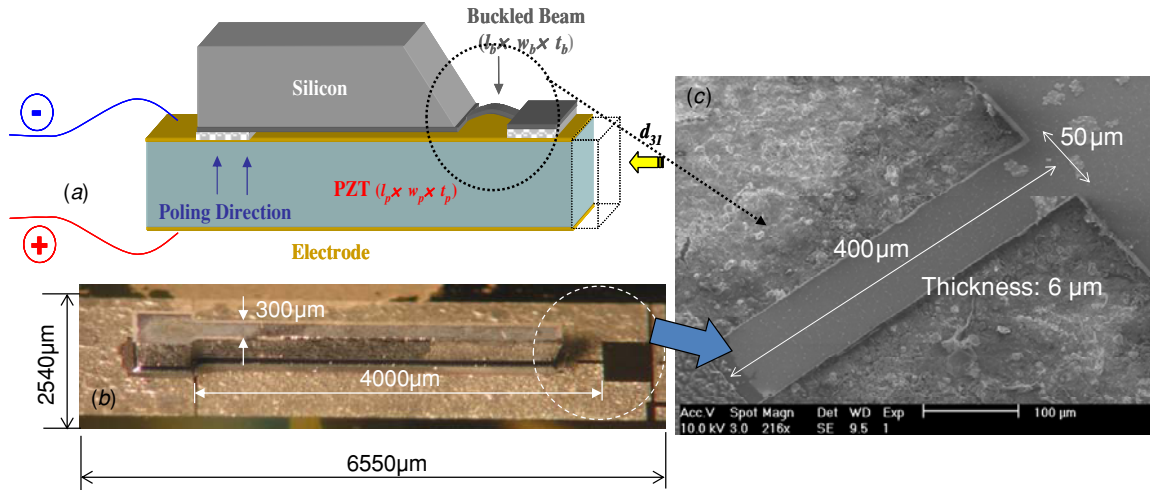
Figure 11. (*a*) Schematic illustration of the flextensional piezoelectric actuator fabricated using the integrative approach. (*b*) Optical photograph of the actual fabricated device and (*c*) scanning electron photograph (zoom) of the actuator of the freestanding silicon structure bonded onto the PZT substrate.

Table 8. Piezoelectric material properties [121–123].

Property	Units	Material				
		Quartz	AlN	LiNbO$_3$	ZnO	PZT
v_a (long)	m s^{-1}	5730	11 350	7267	6070	2700
v_a (shear)	m s^{-1}	4678		3600	2747	
κ^2		0.008	0.065	0.027	0.094	0.18
Q (1 GHz)		27 000	∼1000	100 000	∼1000	100
d_{TE}	μm	2.86	5.42	3.59	2.93	1.25
d_{LFE}	μm	2.34		1.80	1.37	

and resonances (zero impedance) at

$$\omega_r = \frac{v_a}{d}\sqrt{(N\pi)^2 - 8k^2}, \qquad N = 1, 3, 5, \ldots, \qquad (9)$$

where $k^2 = k_t$ (TE) or $-\kappa^2$ (LFE) is assumed small. Typically, TE and LFE resonators are operated at resonance and antiresonance (equations (9) and (8)) respectively. Table 8 shows the thickness required for a fundamental mode 1 GHz resonator constructed of various piezoelectric materials in TE (d_{TE}) and LFE (d_{LFE}) modes under the assumption of pure shear or longitudinal propagation.

The FBAR consists of a piezoelectric membrane suspended over an air gap. Electrodes on the top and bottom faces allow excitation of longitudinal or shear modes depending on the crystal orientation. FBARs provide high electromechanical coupling and excellent integratability and recently resonators with the Q-factor ∼5200 have been demonstrated [4]. FBARs using a composite membrane consisting of piezoelectric and a higher Q-factor substrate layer have also been investigated. Q-factors from 1000–3000 have been reported with ZnO on Si [124] and as high as 5100 for PZT [125]. Unfortunately, the electromechanical coupling is reduced in these devices because the substrate layer is 'dead' without piezoelectric actuation. Composite FBAR devices, however, can be designed to have zero frequency drift with temperature (i.e. TCF = 0) [122]. On the other hand, SMR devices use a piezoelectric layer with top and bottom electrodes on an acoustic Bragg reflector (BR) acting as a mirror to prevent possible energy loss into the substrate from the resonating piezoelectric region. These devices are relatively rugged and easy to fabricate but again suffer from low Q (∼1000) for the same reasons as the FBAR but with additional losses to the substrate.

HBARs provide a high Q-factor by taking the composite FBAR to the extreme limit where the piezoelectric material and electrodes occupy a very small percentage of the resonator volume. Typically, a thick (3 mm), high Q-factor material (e.g. sapphire) is polished to provide parallel faces. Thin (3 μm) piezoelectric material with top and bottom electrodes is mounted on this substrate. Q-factors up to 67 000 have been reported at 1.6 GHz [126]. Unfortunately, the coupling coefficient for this resonator is less than a tenth of 1% and the desired resonator peak is surrounded by spurious resonances at ±8.64 MHz. The general rule of thumb is that the filter percentage bandwidth is about half that of the effective κ^2 of the resonator [127]. Thus, the bandwidth for a 1.6 GHz HBAR filter is exceedingly small (152 kHz).

Clearly, there is a tradeoff between the coupling coefficient and Q-factor in resonators. Thus, a figure of merit (FOM) $\kappa^2 Q$ is often used [124]. The effective piezoelectric coupling coefficient can be described as the ratio of the energy stored in the electric field to the energy stored in the acoustic field. A high coupling coefficient improves insertion loss, and can provide a tradeoff for higher quality factor, in which a small sacrifice in the coupling coefficient can yield an increased figure of merit [4]. The quality factor is the ratio of the stored energy in a network divided by the power dissipated in the network of a given cycle. The FOM for the 1.6 GHz HBAR discussed in the previous paragraph is around 12 whereas the FOM for a 2 GHz SMR is 7 [128]. Thus, using the FOM we can compare the performance of disparate resonator designs. Note that Q is inversely related to frequency and κ^2 is independent of frequency so the FOM is inversely proportional to frequency. The FOM also determines insertion loss for the resonator.
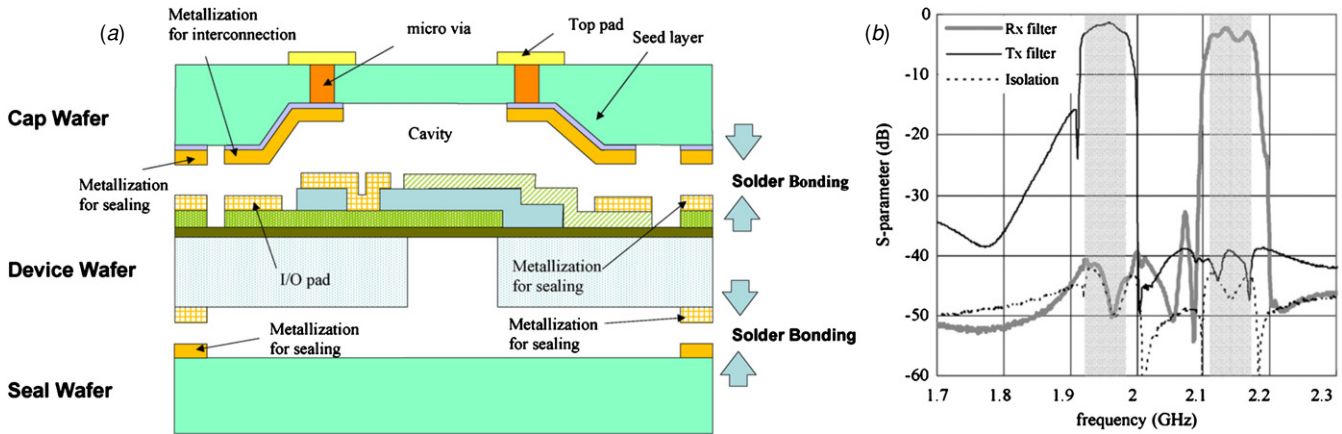
Figure 12. (*a*) The schematic cross-section of the package process and (*b*) measured *s*-parameter of the one-chip duplexer [129].

A critical component in cell phones is the duplexer. It consists of two filters: a transmit filter (*Tx*) and a receive filter (*Rx*). These need to be carefully designed and tuned to result in low insertion loss in their respective bands while maintaining good isolation between the two bands. The Agilent FBAR team, in 2005, formed Avago Technologies, where many innovations in the FBAR filter area have been made [4]. The commercially available ACMD-7403 has a 3 mm by 3 mm footprint and a maximum insertion loss of 2.7 dB in the *Tx* band of 1850.5–1909.5 MHz. Return loss at the transmit port, across the band, is at most −16 dB and the rejection in the receive band is ∼−45 dB. In the receive channel, the maximum insertion loss is 3.2 dB in the *Rx* band of 1930.5–1989.5 MHz. Return loss is at most −13 dB at the receive port and rejection of the transmit channel is almost 60 dB across the whole band.

Researchers Nam *et al* have developed a monolithic one-chip FBAR duplexer which has a 2.5 mm by 2.5 mm footprint, has a maximum insertion loss of 3.1 dB in the *Rx* band of 2110–2170 MHz with an attenuation of over 49 dB and a maximum insertion loss of 2.5 dB in the *Tx* band of 1920–1980 MHz with 39 dB minimum attenuation [129]. Figure 12(*a*) shows the cross-sectional schematic of the fabricated device and figure 12(*b*) shows the *s*-parameters of the *Tx* and *Rx* filters.

6.2. Quartz crystal microbalance

Quartz crystal microbalance (QCM) have been in steady use for a number of years as a convenient tool to determine mass loading of material layers with layer thicknesses ranging well below the monolayer level. A QCM typically consists of a slab of thin, single-crystal, piezoelectric quartz, with very large lateral dimensions in comparison to its thickness, which is sandwiched between two metal electrodes. Application of a sinusoidal electric field using the electrodes sets up a shear wave through the thickness of the quartz and under ideal boundary conditions where no other loading is present; the device exhibits a resonance behavior when the thickness of the quartz slab is half the wavelength of the shear acoustic

wave. Thus, the fundamental resonance frequency of a quartz resonator can be simply given by

$$f_0 = \frac{1}{2t_q}\sqrt{\frac{\mu_q}{\rho_q}}, \qquad (10)$$

where t_q is the thickness of the quartz slab and μ_q and ρ_q are the shear modulus and density of quartz respectively. One of the reasons for the widespread use of quartz resonators in frequency control applications is the exceptionally low phase noise obtained which allows for a precision of few parts in 10^{14} at optimal measurement times [130]. The phase noise is quantitatively specified in terms of the *Q*-factor defined as the half-width at the full maximum of the resonance curve or in terms of energy dissipation factor *D* which is inversely proportional to the decay time constant and is also equal to the $1/Q$-factor.

The resonance frequency is significantly affected by any surface load placed on the quartz crystal including electrode metals. Loading on the resonator surface can be of three types: (i) pure elastic loads (rigid solids), (ii) pure viscous loads (liquids) and (iii) viscoelastic loads (polymers) and/or a combination of any of these. The interaction of the transverse shear wave with these loads has been treated using three fundamental approaches: (i) evaluation of the electrical admittance characteristics upon mechanical perturbations on the resonators [131, 132], (ii) continuum mechanics approach wherein the added material is modeled as a viscoelastic material with associated viscosity and elastic modulus [133, 134] and (iii) the energy transfer model in which the quartz resonator and the deposited film are treated as a compound resonator and energy balance methods are used to evaluate the perturbed characteristics of the resonator [135]. Typically, these approaches are based on a one-dimensional treatment of the problem since the lateral size of the resonators is typically much larger than the relevant dimensions such as the penetration depth of the acoustic waves in the direction perpendicular to the surface of the resonators.

6.2.1. Response of the quartz resonator: elastic loading.
The concept of mass measurement using a resonating quartz crystal was first presented by Sauerbrey [136]. For a resonator

with a resonance frequency of $f_0(0)$ with no attached mass to it, the frequency change, Δf, upon addition of a rigid mass of small thickness in comparison to the quartz resonator thickness and under no-slip condition can be given by

$$\Delta f = -\left(\frac{2f_0^2(0)}{A\sqrt{\rho_q \mu_q}}\right)\Delta m = -\left(\frac{1}{t_q^2 A (2\rho_q)}\sqrt{\frac{\mu_q}{\rho_q}}\right)\Delta m, \quad (11)$$

where μ_q is the shear modulus of the crystal (2.947×10^{10} N m^{-2} for *AT*-cut quartz), ρ_q is the density of quartz (2.648×10^3 kg m^{-3}), t_q is the thickness of the quartz crystal and A is the area of the electrode on the quartz crystal. The negative sign indicates a reduction in the resonance frequency upon mass loading. The most common commercially available quartz crystal microbalances have a resonance frequency of 5–10 MHz. These typically consist of 25.4–12 mm diameter and 333–167 μm thick *AT*-cut quartz disks with gold electrodes on each face and exhibit a mass sensitivity of 17.7–4.42 ng cm^{-2} Hz respectively. Based on empirical data, the smallest frequency noise in an *AT*-cut quartz resonator has been approximated to be $\sim 1.2 \times 10^{-20} \cdot f_0^2$ [137]. Thus, the highest mass resolution that can be achieved by a given QCM can be calculated by dividing this expression by the mass-sensitivity factor in equation (11), i.e.

$$\Delta m_{\text{ultimate}} = 0.6 \times 10^{-20} * A\sqrt{\rho_q \mu_q} = 5.3 \times 10^{-15} A, \quad (12)$$

where $\Delta m_{\text{ultimate}}$ is given in g and area A is given in cm^2 units. Thus, it is clear that decreasing the area of the resonator will improve the absolute mass sensitivity of the QCM. For instance, if the diameter of a resonator is reduced from 1 cm to 0.001 cm, an absolute mass resolution in the range of zeptograms (10^{-21} g) can be realized.

In finite electrode-sized resonators, energy trapping is necessary to maintain a high Q-factor which is determined by the effectiveness of the total internal reflection of vibrations at the edge of the electrodes to confine the acoustic energy to within this region only. Excessive decrease in the electrode diameter, however, will result in acoustic energy leakage and poor confinement of energy resulting in small Q-factors. Furthermore, as the quartz resonator thickness is reduced the electrode diameter also must be reduced in order to effectively suppress spurious modes. These opposing requirements entail a design compromise. Our results have shown that for 50–90 MHz resonators with 100 nm of gold electrodes on both faces, the optimal electrode diameter ($2r_q$) to resonator thickness (x_q) ratio is $\sim$10–20. Large deviations from this value either way results in resonators with poor characteristics.

6.2.2. Response of the quartz resonator: viscous loading.
When used for applications such as biosensing and electrochemical studies, where one of the resonator surfaces is in contact with a liquid medium, the viscous drag effects need to be considered and now determine the ultimate device performance. Behavior of quartz resonators under purely viscous loading was first reported by Kanazawa and Gordon in 1985 [138]. Under such conditions, the fundamental mode QCM frequency shift is given by

$$\Delta f = -\frac{f_0^{3/2}}{\sqrt{\pi \rho_q \mu_q}}\sqrt{\rho_L \eta_L}, \quad (13)$$

where ρ_L and η_L are the viscosity and density of the liquid, respectively. For operation in liquids, the mass resolution of the QCM is modified and can be given as [139]

$$\Delta m_{\text{liquid}} = 5.64 \times 10^{-8} \frac{\sqrt{\rho_L \eta_L}}{\sqrt{f_0}} A, \quad (14)$$

where all quantities are specified in SI units. In the case of liquid operation, it is quite clear that a high-frequency resonator is likely to provide a higher mass resolution. However, often in liquid applications, we are interested in measuring viscosity and density changes in liquid rather than mass changes. The ultimate density/viscosity resolution of a quartz resonator can be given by the expression

$$\frac{\Delta \eta_L}{\eta_L} + \frac{\Delta \rho_L}{\rho_L} = 4 \times 10^{-7}. \quad (15)$$

Since most liquid experiments are accompanied by simultaneous changes in the density and the viscosity of the liquid, equation (15) gives the combined minimum resolution in both parameters. In liquid medium applications, the shear wave rapidly damps out as it travels through the thickness of the liquid and consequently the QCM typically samples a layer of thickness equivalent to the decay length $\delta = (\eta_L/\pi \rho_L f_0)^{0.5}$ [140]. For a commercial 5 MHz QCM, the typical decay length in water is $\sim$250 nm, which is large in comparison to the thickness of molecular or even polymer and biomolecular (e.g. proteins) films which can be in the thickness range of 10–50 nm. As a result, a commercial QCM not only samples the adsorbed film but is also significantly affected by the viscous liquid layer above it. Small changes in the viscoelastic properties of adsorbed layers are often masked by the viscous effects from the liquid overlayer. However, if the QCM thickness is decreased, its fundamental resonance frequency increases inversely as a function of the thickness of the quartz and thus the decay length in liquid also decreases consequently. For example, if the thickness of a quartz resonator is decreased from 330 μm (commercial 5 MHz resonator) to 24 μm (miniaturized 66–69 MHz resonator), the decay length in water is reduced to $\sim$68 nm. These factors are critical to the improved abilities of miniaturized devices to probing viscoelastic characteristics of adsorbed layers compared to standard commercial QCMs.

6.2.3. Response of the quartz resonator: viscoelastic loading in a liquid ambient.
The QCM frequency shift resulting from the deposition viscoelastic layer in a viscous liquid ambient can be analyzed using a continuum mechanics approach, for example as developed by Kasemo and coworkers [134]. In order to model this situation, the QCM surface is considered to be in intimate contact with a layer of continuous viscoelastic slab with an infinitely thick Newtonian liquid overlayer on one of its surfaces. Under the assumption that the thickness of the bulk liquid layer is much larger than the decay length of the acoustic wave in the liquid, the frequency and Q-factor changes with respect to liquid loading conditions can then be written as

$$\Delta f \approx -\frac{1}{2\pi \rho_q t_q} \sum_{n=1,2,...} \left(t_n \rho_n \omega - 2t_n \left(\frac{\eta_L}{\delta_L}\right)^2 \frac{\eta_n \omega^2}{\mu_n^2 + \omega^2 \eta_n^2}\right)$$
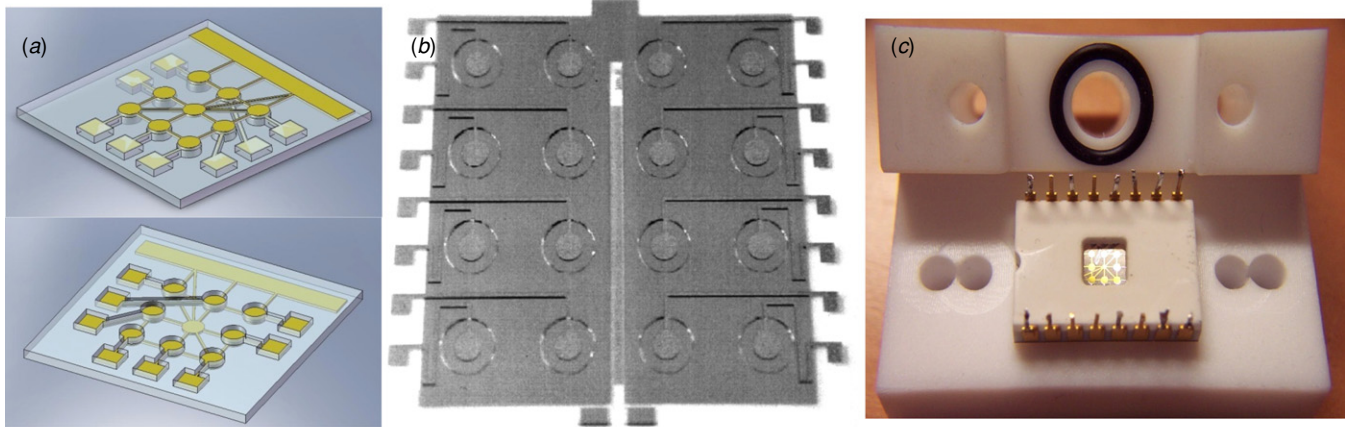
$$(16)$$

Figure 13. (*a*) Schematic illustration of the top view (liquid and/or viscoelastic loading surface) and backside view of a typical micromachined quartz crystal microbalance array consisting of eight pixels [144], (*b*) 22 MHz quartz resonator array fabricated and demonstrated by the Braunschweig group in Germany [22] and (*c*) packaged 66 MHz device in a ceramic dual in-line package placed in a liquid test cell from our recent work [144].

$$\Delta Q \approx -2\pi f_0 \rho_q t_q \frac{\sum_{n=1,2,.}\left(2t_n \frac{\mu_n \omega}{\mu_n^2 + \omega^2 \eta_n^2}\right)}{1 + \sum_{n=1,2,.}\left(2t_n \left(\frac{\eta_L}{\delta_L}\right)\frac{\mu_n \omega}{\mu_n^2 + \omega^2 \eta_n^2}\right)}, \qquad (17)$$

where $\rho_q = 998.21$ kg m^{-3} is the density of quartz, t_q is the thickness of the resonator, μ_n is the elastic modulus, η_n is the viscosity, t_n is thickness of the nth layer adsorbed on the resonator and η_L and δ_L are the viscosity and penetration depth of the acoustic wave in the bulk liquid respectively.

Micromachined quartz resonator arrays have been fabricated by several researchers [96, 98, 141]. In one of the earliest reports on a micromachined QCM, Smith and Senturia [96] interfaced a 22 MHz QCM array with a resonator driver and multiplexer chip and demonstrated the temperature drift compensated system for chemical sensing application. And more recently, Rabe *et al* have demonstrated 22 MHz micromachined QCM arrays (figure 13(*b*)) [22] and used it for label-free analysis of the affinity reaction between a ligand and its receptor [142]. In their work recombinant human bone morphogenetic protein-2 (rhBMP-2) produced in high-cell-density cultures was chosen as ligand, and binding to the specific extracellular binding domain of the human bone morphogenetic protein (BMP) receptor type IA (BMPR-IA) and also to a specific monoclonal anti-human BMP-2 antibody was investigated [142]. The most detailed reports of the performance of single and resonator arrays of the QCM are in the 20–30 MHz region [96, 98, 142] and more recently on 62–66 MHz single and resonator arrays from our group [101, 143, 144]. Figure 13(*a*) shows the schematic illustration, the resonator array fabricated by our group [22], and figure 13(*c*) a photograph of the packaged device and liquid test cell respectively [144].

Figure 14 shows the admittance (Y_e) characteristic of one of the fabricated devices in air. From the peak of Re(Y_e), a resonance frequency of 66.063 MHz, a motional resistance of 47 Ω and a Q-factor of $\sim$25 000 can be deduced. This shows that it is possible to maintain excellent resonator characteristics even after miniaturization. We have used these resonators for (i) demonstrating array level
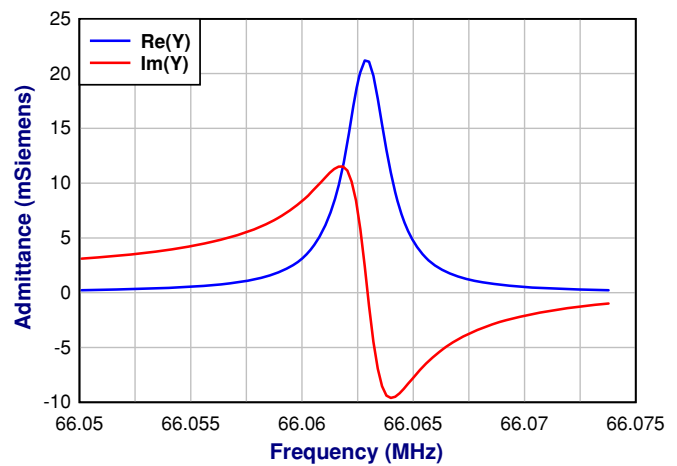

Figure 14. Admittance characteristics of a miniaturized quartz crystal resonator operating at $\sim$66 MHz in air [144].

biosensing applications [143], (ii) studying the viscoelastic and material properties of monolayers of biomaterials [101, 145] and diffuse double layer in voltammetry scans [146] and (iii) studying multilayers of biomolecular films [144].

6.3. SAW-resonator-based chemical and biochemical sensors

Surface acoustic wave devices have been commercialized for high-frequency RF filter applications for the last several decades and more recent efforts have focused on the development of commercial (bio)chemical sensor applications. This section will focus on the chemical and biochemical applications of 'surface-launched' acoustic wave mode devices. These sensors are based upon the detection of the changes in acoustic propagation characteristics of surface-launched waves typically in piezoelectric materials. All these devices have similar surface transducers that generate the acoustic wave at the surface of the substrate although the wave may propagate either through the bulk of the material or on the surface depending upon the exact construction of
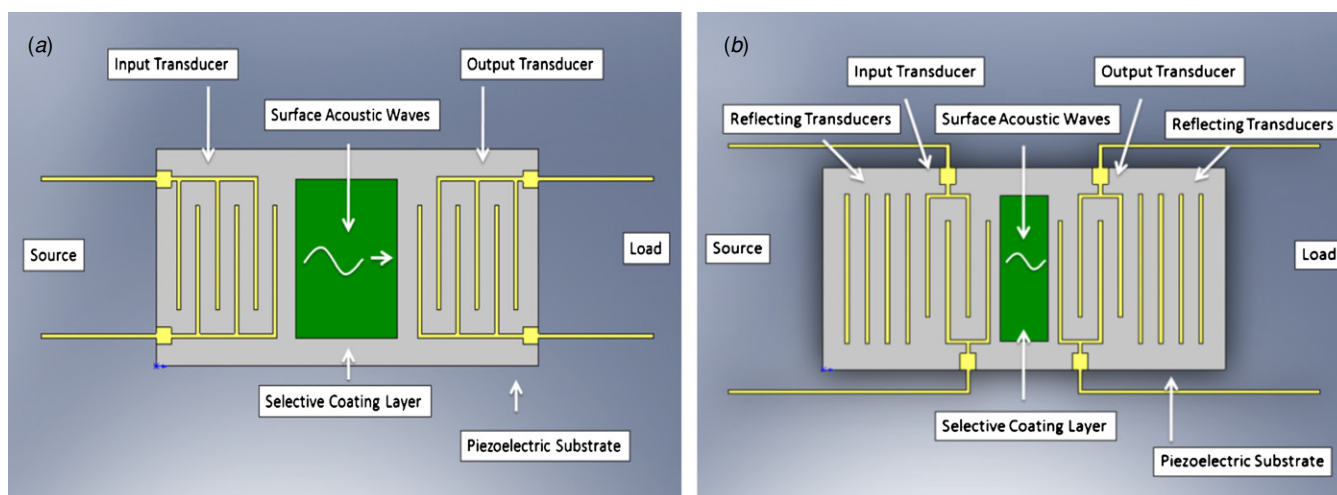
Figure 15. Two-port delay-line-based sensor and (*b*) two-port resonator-based sensor.

Table 9. Surface acoustic waves and their characteristics.

	Particle displacement [149]	Operating frequency (MHz) [149]	Phase sensing [149]	Plate thickness [149]	Mass sensitivity $((Hz\ MHz^{-1})$ $(ng\ cm^{-2})^{-1})$
SAW	Transverse and parallel	30–500	Gas	N/A	0.2
FPW (Lamb)	Transverse and parallel	2–7	Gas, liquid	Few μm	0.379 [161]
SH-APM	Transverse	25–200	Gas, liquid	Hundreds of μm	0.019
STW (Love, SH-SAW)	Transverse	200–500	Gas, liquid	Few μm	0.18

the sensor. Table 9 outlines different types of surface acoustic waves and their characteristics.

Traditional surface acoustic wave devices utilize Rayleigh waves, in which particle displacement is normal and parallel to the surface of the substrate. These types of waves function well in gaseous or vacuum environments; however when immersed in liquid, compressional waves are created causing significant attenuation which precludes them from liquid sensing applications [147]. Flexure plate waves (FPWs), however, produce compressional waves that are not coupled in liquids; thus, they do not significantly attenuate the acoustic energy making them well suited for liquid sensing applications [148]. Similarly, the shear horizontal waves generated from the shear horizontal acoustic plate mode (SH-APM) and surface transverse waves (STWs) do not radiate energy into liquids. The FPW and STW devices are comprised of a thin piezoelectric plate of thickness less than the acoustic wavelength, typically a few micrometers. The SH-APM is generally on the order of hundreds of micrometers. Although these waves are generated from transducers on the surface, the waves travel through the bulk of the piezoelectric plate. An excellent review of different types of 'surface-launched' acoustic waves can be found in [149]. SAW-based sensors, utilizing the Rayleigh wave, have been used to detect chemical and biological molecules such as volatile organic compounds (VOCs) [150], CO_2 [151], humidity [152], ammonia [153], drugs [154], microbials [155] and DNA [156]. Similar to

thickness shear resonators (TSRs), FPW, shear horizontal SH-APM and STW-based sensors have displayed better mass sensitivity and can be used in liquid sensing applications where traditional Rayleigh SAW devices are unsuitable [157, 158]. A more detailed description of different wave modes is given in [157], and for a more detailed review of all piezoelectric acoustic wave sensing technology, the reader is referred to [159].

Two types of configurations are generally used for SAW-based sensing applications: delay line and resonator. The delay line usually has two ports: an input and output inter-digital transducer (IDT), and an active area where the sensing takes place. The input IDT generates a propagating acoustic wave, which travels through the active area, and then is received after a time delay by the output IDT. The difference in frequency is used to sense a mass loading in the active area. A two-port resonator is very similar to this configuration except that on either side there are reflector-IDTs and the device uses a standing wave rather than a propagating wave [154, 160]. Schematic illustration of these two types of configurations are shown in figure 15.

While the most common piezoelectric material used in SAW and FPW devices is quartz [154], lithium niobate and tantalate [162], AlN [156], ZnO [149], and PZT [163] have also been used. Surface-launched acoustic wave chemical and biological sensors possess many advantages over other types of sensing. The mass sensitivity of SAW-based sensors is

superior to BAW sensors because the energy in the surface acoustic wave is maximized at the surface [148]. With higher operating frequencies, greater sensitivity can be achieved at the expense of more complicated electronics. The FPW mass sensitivity is reported to be an order of magnitude higher than an equivalent SAW, and also uses lower frequencies which require less complicated electronics and lower noise levels [161]. Both types of devices can be configured with dual delay lines on the same chip, in which one can be used as a reference and another as the sensor to correct for undesired effects such as temperature drift [150]. The focus of recent work in surface-launched acoustic wave chemical and biological sensors has been on coatings and applications [164, 165]. Using AlN and PZT thin films, higher resonance frequencies and improved electromechanical coupling coefficients in FPW devices have been demonstrated [163, 166]. In summary, surface acoustic wave devices offer a sensitive technique for studying changes in the mass, charge, viscoelastic properties and acoustic coupling effects occurring at the sensor (solid)–analyte (liquid) interface [148].

When a surface acoustic wave device interacts with fluid media, such as in biosensing applications, acoustic energy dissipation leads to a mode conversion from Rayleigh to leaky SAW. This mode conversion results in longitudinal wave propagation in the fluid domain which, if of sufficiently high intensity, results in a net pressure gradient along its direction of propagation thereby inducing fluid flow. The fluid motion resulting from the attenuation of sound waves induces acoustic streaming. Recent experimental work has shown that the Rayleigh waves produced in lithium niobate and in lithium tantalate can be effectively used to clean the sensor surface through the use of acoustic streaming [167–169]. Based on the wave modes, the acoustic streaming phenomenon can be utilized for micro-transport of the target analyte to specific locations or onto sensor surface for its concentration and/or removal of the non-specifically bound molecules away from the surface. Effects of acoustic energy manipulation through the use of etched disk on the wave propagation and on the streaming velocity fields are an emerging field of application for surface acoustic waves.

6.4. Ferroelectric thin film infrared detectors

Thermal infrared detectors are broadband detectors and can be operated at room temperature without cooling [170]. In general, they have lower detectivity and slower response time in comparison to cooled semiconductor photonic detectors. However, micromachined thermal detectors owing to their small thermal mass and good thermal isolation demonstrate much improved performance [171]. These detectors can be designed to operate near the room temperature thermodynamic noise limit arising from the thermal conductance fluctuation between the sensing element and the supporting substrate [170]. The advent of focal plane arrays (FPAs) comprising such miniaturized thermal sensors has made it possible to find low cost room temperature infrared imaging cameras. Much of this research was funded by the United States Department of Defense. The two main technological approaches to infrared

detectors was taken by (i) Honeywell based on a vanadium-pentaoxide-based microbolometer [172] and (ii) Raytheon based upon barium strontium titanate (BST) based pyroelectric detectors. An excellent review on the state of art in the field of infrared detectors and arrays is presented by Rogalski [173] and a historical review of the development of these devices is given more recently by Bogue [174].

Pyroelectric crystals exhibit spontaneous electric polarization which can be measured as a charge or voltage at electrodes attached to the sample. However at constant temperature the internal charge distribution is neutralized by free electrons and stray surface charges, so that no voltage is detectable. If the temperature of the crystal is varied rapidly the internal dipole moment will change, producing a transient voltage. This pyroelectric effect is exploited to produce sensitive detectors of modulated infrared radiation, operating at ambient temperature. Temperature-sensitive pyroelectric crystals include certain ferroelectric crystals such as triglycine sulfate TGS, BST, lanthanum-doped lead zirconate titanate (PLZT) and $LiNbO_3$.

Pyroelectric detectors are capacitors, having metallic electrodes applied to opposite surfaces of the temperature-sensitive ferroelectric crystal or film. Modulated radiation absorbed by the detector causes the temperature of the crystal, T, to fluctuate by ΔT. An instantaneous temperature change ΔT of the pyroelectric crystal establishes an instantaneous charge ΔQ on the external electrodes given by

$$\Delta Q = pA\Delta T, \tag{18}$$

where p is known as the pyroelectric coefficient of the material and A is the area over which the incident radiation is absorbed. Thus, the photocurrent is proportional to the rate of change of temperature, i.e.

$$I_s = pA\frac{d(\Delta T)}{dt}. \tag{19}$$

Pyroelectric infrared detectors have been reviewed by Putley [175] and a more recently by Muralt [176]. In addition to the pyroelectric effect, near the transition temperature (Curie temperature) the dielectric constant of the material is also observed to increase dramatically. This second effect is used to generate signals, for example, in Raytheon's BST technology. Since the BST in this case is designed to operate at the ferroelectric phase transition, the detector temperature must be maintained within a range of about 0.2 °C for maximum signal [177]. In addition, all pyroelectric detectors require some kind of chopping action for detection. The original Texas Instruments approach has been to use the integrative hybrid approach to realizing these devices using solder bump technique couple the BST detector array with the readout electronics chip. Using this technology, they were able to demonstrate as low as 38 mK noise equivalent temperature difference (NETD) using $f/1$ optics [119].

Modern imagers based upon pyroelectric detectors are typically implemented using micromachining techniques. Deposition of thin film ferroelectric materials has allowed the construction of better thermally isolated IR sensor structures. The microbridge structures offer better thermal isolation and lower cost products through batch fabrication techniques
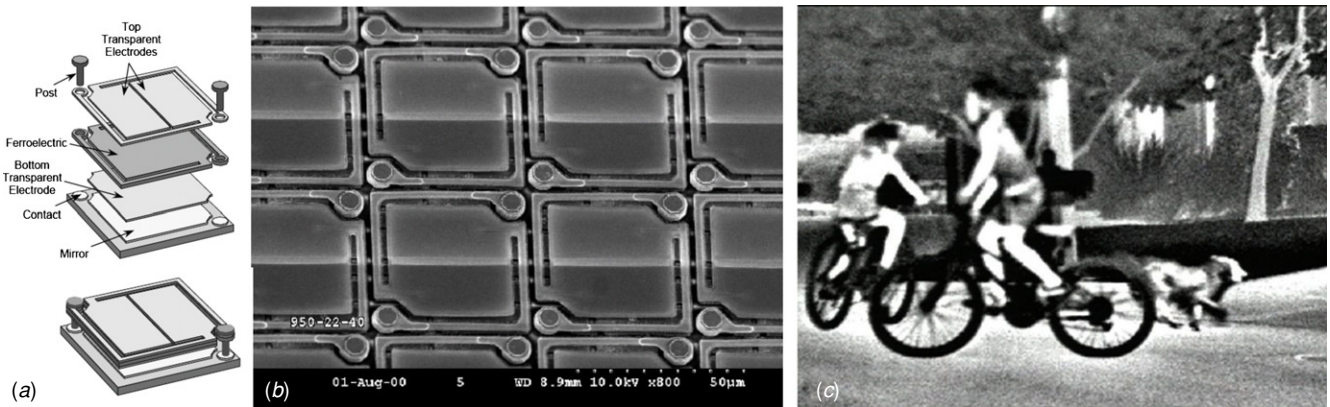
Figure 16. (*a*) Exploded view of a TFFE-based pyroelectric detector pixel, (*b*) SEM photograph of a part of 330×240 pixel IR imaging array and (*c*) an IR image obtained using the TFFE detector using $f/1$ optics [177].
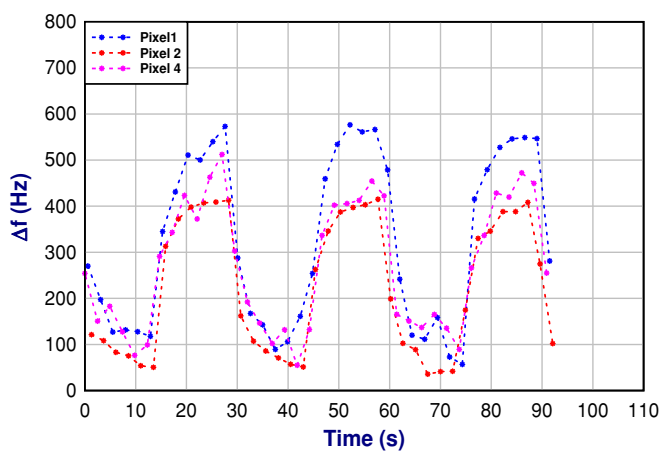

Figure 17. The simultaneous response of 3 quartz resonator pixels upon absorption of infrared radiation from a broad band lamp source modulated at a frequency of 33 mHz is shown [184].

[177, 178]. The thin film ferroelectric (TFFE) technology based upon calcium lead titanate (CLT) and PLZT thin films has been commercialized by Texas Instruments. Unlike the BST detector, the CLT/PLZT-based IR detectors utilize the direct pyroelectric effect which does not require the temperature of the detectors to be accurately controlled. Figure 16(*a*) shows the exploded view of the thin film CLT pyroelectric detector pixel, figure 16(*b*) a SEM photograph of the section of a 320×240 pixel array, and figure 16(*c*) shows a thermal image obtained using the TFFE imager. Although the NETD of the detector was only 0.21 °C, the images show very high quality which has been attributed to the high modulation transfer function (MTF) of these detectors [177]. More recent detectors have been fabricated using PLZT films ($p \sim$ 15–20 nC °C^{-1} cm^{-2}, $\varepsilon \approx 350$, tan$\delta \approx 0.03$) [179]. The NETD of the 48.5 μm pixels from this material has been reported to be ~80–90 mK.

More recently, thickness shear mode resonators from quartz have been proposed and demonstrated as sensitive infrared detectors [137, 180–183]. The unprecedented temperature sensitivity along with the low noise performance that can be achieved in quartz crystal oscillators is the principle of operation of several thermal sensors based on acoustic

waves. Harmour *et al* demonstrated an IR sensitivity of 107 ppm mW^{-1} allowing for a detection limit of 1 μW. They were able to achieve the proposed sensitivity in a 88 mm^2, 360 μm thick, *Y*-cut quartz resonator with $f_0 =$ 5.1 MHz [181]. Using a 500 K blackbody IR source, Kim and Vig [182] achieved a detectivity $D* = 8 \times 10^7$ cm Hz$^{1/2}$ W^{-1} using an *AC*-cut quartz with $f_0 = 160$ MHz and a detector area of 500 μm $\times$ 500 μm. We have also reported the fabrication and performance of a micromachined *Y*-cut quartz-resonator-based thermal infrared detector array. 1 mm diameter and 18 μm thick (90 MHz) inverted mesa configuration quartz resonator arrays with excellent resonance characteristics have been fabricated by RIE etching of quartz [184]. Figure 17 shows the multiplexed response of 3 of an 8 pixel quartz resonator array to pulsed infrared irradiance at a frequency of 33 mHz. For the three resonators shown, an average frequency change of 400 Hz was observed for an incident radiation density of 3.15 mW cm^{-2}. Measuring the noise in 1 Hz bandwidth, a D^* value of 3.73×10^6 cm Hz$^{1/2}$ W^{-1} was estimated [184]. The time constant of the resonator pixel was calculated to be 7.2 ms [184]. However, the response time measurements were found to be limited by the use of slow measurement time of the impedance scans and the undesired heating of the quartz substrate and are being currently addressed.

6.5. Piezoelectric accelerometers and angular rate sensors

6.5.1. Piezoelectric accelerometers. Piezoelectric materials can be integrated into micromechanical structures and configured for accurate inertial measurements. Using the direct piezoelectric effect, these devices can be used as sensitive accelerometers, specifically for vibration level sensing and for monitoring temporal variations in acceleration. Vibrating structures made from piezoelectric resonators can also be used as gyroscopes for angular rate sensing or accelerometer applications. The concept of piezoelectric accelerometer was proposed as early as 1964 when it was realized that application of stress changes the resonance frequency of a quartz oscillator [185].

Figure 18 shows some of the micromachined accelerometers that have been fabricated by various groups.
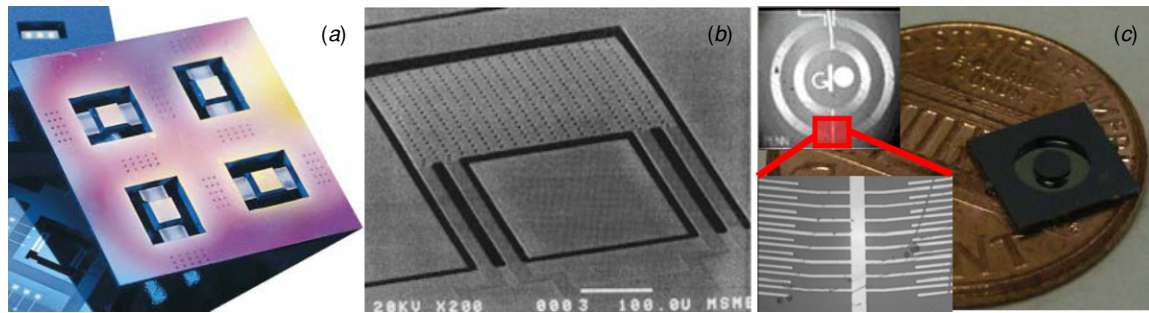
Figure 18. (*a*) Bulk micromachined ZnO accelerometer based on a clamped–clamped structure. The silicon proof mass was etched using KOH (from [204]), (*b*) surface micromachined ZnO accelerometer released using XeF$_2$ (from [187]) and (*c*) bulk micromachined accelerometer using interdigitated electrodes. The inset shows the front side of the accelerometer with zoom-in of the interdigitated electrodes (from [197]).

Table 10. Comparison of some of the piezoelectric accelerometers reported in the literature.

Sensing material	Fabrication method	Sensitivity	Resonance frequency (kHz)	Comments
ZnO [186]	1.7 μm sputtered ZnO	~22 μV g^{-1}	20–40	Bulk micromachined. Integrated with MOS Readout IC. Range: 10 000 g
ZnO [204]	1 μm thick sputtered ZnO	1.75 mV g^{-1}	4.5	Bulk micromachined using KOH etching. Proof mass of 3 mg was used
ZnO [187]	0.5 μm sputtered ZnO	44.7 mV g^{-1}	1.03	Surface micromachined using XeF$_2$ substrate silicon etching. Stress compensation is achieved using tensile Si$_3$N$_4$ film
ZnO [189]	0.3 μm sputtered ZnO on 3.7 μm parylene	7 mV g^{-1}	0.1	ZnO film sputtered on the parylene structural layer. The device is configured as a bimorph sensor
AlN [27, 190]	1.1 μm thick sputtered AlN film on the Mo electrode	5.2 pC g^{-1} (10.35 mV g^{-1})	~1.1	A new tapered beam design clamped at the nodal point is used to maximize the signal-to-noise ratio
PZT [195, 196]	1.5–7 mm thick sol–gel PZT films	7.60–0.77 pC g^{-1}	3.7–35.3	Bulk micromachined. A circular membrane design with d_{31} coefficient was used
PZT [197]	0.6 μm PZT on 0.5 μm ZrO$_2$ deposited by sol–gel	6.5 mV g^{-1}	15.5	Bulk micromachined. Identical to the previous device except uses interdigitated electrode (d_{33}) coefficient
PZT [191]	Bulk PZT hybrid device dielectric constant $\varepsilon_r \sim 2600$	3.2 pF g^{-1}	14 kHz	Novel capacitive device exploiting the high dielectric constant of bulk PZT and fringing field coupling via PZT
PVDF [200]	Macro-scale device. 110 μm thick PVDF film	2.15 V g^{-1}	~100 Hz	Proof mass is 184 g. The device is machined and assembled

These accelerometer designs exploiting the direct piezoelectric effect have been made from various materials such as ZnO [186–189], AlN [27, 190], PZT [191–197] and PVDF [198–203]. Typically, these accelerometers use a proof mass in the range of 1–10 mg made out of bulk micromachined silicon which is connected to the silicon substrate frame using flexural structures on which the piezoelectric thin film is integrated using several of the deposition techniques discussed earlier. Table 10 compares the performance of some of the micromachined piezoelectric accelerometers reported in the literature. Aoyagi *et al* [191] presented a novel concept for acceleration sensing based upon the change in capacitance due to change in fringing field coupling in an interdigitated capacitor-parylene proof mass located in proximity to a high dielectric constant $\varepsilon_r \sim 2600$ bulk PZT substrate.

The hybrid integration avoids micromachining of PZT and uses micromachining processes for patterning the parylene freestanding structure and proof mass.

6.5.2. Scaling and sensitivity limits of a piezoelectric accelerometer. In this section, we will explore scaling-based sensitivity limits for piezoelectric accelerometers. A simple schematic model of a piezoelectric accelerometer is shown in figure 19. The accelerometer consists of a micromachined silicon cantilever with a proof mass at its tip. The cantilever of length *l* has a rectangular cross-section of $w \times t$. The proof mass is assumed to act as a point load at the tip. An acceleration of 1*g* (9.81 ms^{-2}) will result in the bending of the
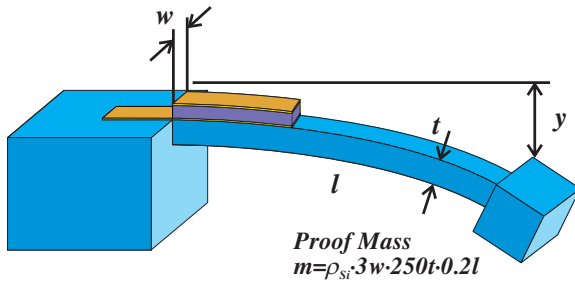
Figure 19. Schematic model of the cantilever-based piezoelectric accelerometer.

cantilever and from beam theory, the deflection y can be given by [205]

$$y = \frac{Fl}{2Y_{Si}I} x^2 \left(1 - \frac{x}{3l}\right),\qquad(20)$$

where $F = m \times g$ is the force, m is the mass of the proof mass, Y_{Si} is the Young's modulus of silicon and I is the moment of inertia of the cantilever beam which can be given by $I = wt^3/12$. The top surface of the cantilever will experience a tensile stress, which can be given by

$$\sigma_x = 6\frac{mg}{wt^2}(l - x).\qquad(21)$$

If the cantilever is coated with an extremely thin layer of a piezoelectric material sandwiched between the two electrode layers in such a manner that the presence of this layer does not significantly perturb the elastic characteristics of the silicon cantilever beam, then to the first approximation, the amount of charge that will be generated in response to this force is given by

$$Q_{Out} = d_{31} \left(\frac{Y_{Piezo}}{Y_{Si}}\sigma_x\right) wl_1,\qquad(22)$$

where Y_{Piezo} is the Young's modulus of the piezoelectric material and it has been assumed that the piezoelectric layer covers the entire width of the cantilever and up to a length l_1 from the clamped end. If the device is being used as voltage source, then the signal voltage can be calculated as $V_{Out} = Q_{Out}/C = Q_{Out} \times t_1/\varepsilon wl_1$, where C is the parallel plate capacitance of the piezoelectric sensing layer, ε is the permittivity of the piezoelectric layer and t_1 is its thickness which is typically around $t_1 = t/10$ to maintain our assumption of insignificant perturbation of the mechanical characteristics of the silicon beam. The sensitivity which is defined as the voltage output per $1g$ of acceleration can now be given as

$$\text{Sensitivity} = \frac{V_{Out}}{g} = 6\frac{d_{31}}{\varepsilon}\frac{Y_{Piezo}}{Y_{Si}}\frac{mt_1}{wt^2}(l - x).\qquad(23)$$

Thus for isometric scaling, i.e. where all dimensions are equally reduced, we can see that the sensitivity will scale as L^2. In this scaling approach, we have assumed that the piezoelectric and dielectric properties of the materials are invariant under scaling. This makes intuitive sense since isometric scaling of the accelerometer is going to decrease the proof mass as L^3 thereby decreasing the signal into the sensor. However, for the very same reason microsensors are more effective for impact and shock sensing. Although a

steady stress level on a piezoelectric material is expected to produce a constant charge, practical sensors inevitably have loss mechanisms built in them which result in the eventual leakage of such charge build-up. Therefore, piezoelectric sensors are typically configured as *ac* or transient-response sensors.

For the piezoelectric sensor, the limits for miniaturization come from two different aspects: (i) material considerations and (ii) structural considerations. In order to determine the ultimate sensitivity given by equation (23), the design of the accelerometer requires the specification of the piezoelectric film with respect to the cantilever dimensions. To continue this analysis further, the following assumptions are made: (i) the accelerometer consists of a cantilever beam of length l, width w and thickness t and is coated with a piezoelectric film from the clamped end to a length l_1 and has the same width as the cantilever, (ii) Euler beam theory can be used to calculate the beam deflection and surface stress on the micromachined silicon structure with a proof mass attached at the tip, (iii) the piezoelectric stress sensing film is assumed to be much thinner than the silicon structural layer and therefore perturbs its deflection characteristics minimally, (iv) the proof mass can be considered as a point load on the cantilever structure when subjected to acceleration, (v) the primary sources of noise in the structure arise due to random thermal fluctuations of the micromechanical structure and due to dielectric loss through the piezoelectric film [206]. Furthermore we will assume that the proof mass is made out silicon, of length $0.2l$ (limited by point load approximation), width of $3w$ and thickness of 500 μm (typical thickness of a 4″ silicon wafer). Now if we consider the case of a PZT accelerometer, the thinnest PZT layers that have been shown to have the highest electromechanical coefficients of $d_{31} \sim 120$ pC N^{-1} are currently around 200 nm thickness [16]. Miniaturizing PZT films below this thickness leads to less than optimal performance figure of merit and will therefore degrade the performance of the fabricated accelerometers. With this thickness as the limit of the PZT film for miniaturization, we can then define the minimum silicon flexural beam thickness to be 2 μm (i.e. 1:10 ratio).

Thus, the average voltage signal due to an acceleration of $1g$ can be given by the expression

$$V_{Signal} = 90\frac{\rho_{Si}d_{31}}{\varepsilon}\frac{Y_{PZT}}{Y_{Si}}l\left(l - \frac{l_1}{2}\right)g,\qquad(24)$$

where ρ_{Si} is the density of silicon and d_{31} and ε are the piezoelectric coefficient and permittivity of the PZT film respectively. The contribution to noise in the accelerometer arises from two independent sources: (i) due to random thermal fluctuations in the cantilever structure and (ii) due to the loss through the piezoelectric capacitor. The thermal fluctuation noise can be given by [206]

$$V_{thermal} = 0.043\frac{d_{31}}{\varepsilon}\frac{Y_{PZT}}{Y_{Si}}\sqrt{\frac{t}{wl}}\sqrt{Yk_BT}\left(1 - \frac{l_1}{2l}\right),\qquad(25)$$

where Y_{PZT} and Y_{Si} are the Young's moduli of PZT and silicon respectively. The PZT film parallel plate capacitor noise,
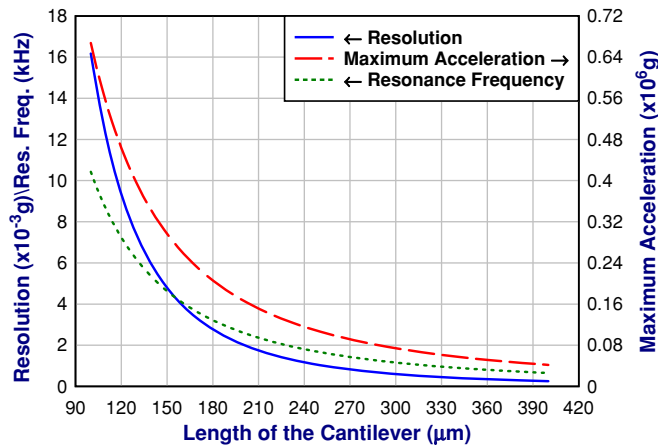
Figure 20. The ultimate resolution, bandwidth and maximum-*g* tolerance that can be achieved as a function of length for a micromachined piezoelectric cantilever-type accelerometer under the assumptions discussed in the text.

Figure 21. Schematic drawing of a typical tuning fork gyro design used by Systron Donner division of BEI Technologies made out of a *z*-cut quartz crystal.

arising due to the leakage of the capacitor dielectric, termed as piezoelectric noise, can be given by

$$V_{\text{piezo}} = \sqrt{\frac{4k_B T \tan \delta}{\omega C}}, \tag{26}$$

where C and $\tan \delta$ are the capacitance of the device and the loss tangent of the PZT film respectively. The nominal value of $\tan \delta$ for the PZT film is ~0.02. Thus, the total noise is given by

$$V_{\text{Noise}} = \left(V_{\text{thermal}}^2 + V_{\text{piezo}}^2 \right)^{0.5}. \tag{27}$$

Based on the signal to total noise relationship (ratio of equation (24) to equation (27)), we can now calculate the length l_1 of the piezoelectric layer that will result in a maximum signal-to-noise ratio. This gives a value for $l_1 = \frac{2}{3}l$. Using these values for the piezo film, the ultimate performance of a cantilever-based piezoelectric accelerometer can now be calculated. Figure 20 shows the noise-equivalent acceleration (i.e. resolution), resonance frequency (bandwidth) and the maximum *g*-force tolerance of the device. These limits which do not consider the noise associated with electronics are very competitive with respect to the Analog Devices accelerometer performance specifications for ADXL 335 [207].

6.5.3. Piezoelectric gyroscopes. Gyroscopes are used to detect the rate of rotation of an object and use Coriolis force effects that arise in rotating frames of reference for such sensing. The magnitude of the Coriolis force vector F_C arising in a continually rotating system can be given by

$$\vec{F}_C \cong 2m\vec{\Omega} \times \vec{V}_R, \tag{28}$$

where m is the mass of the object, V_R is the particle velocity (vector) relative to the rotation axis and Ω is the angular velocity vector of the rotation axis (in $^\circ$ s^{-1}) and $\times$ denotes the cross-product operator. In order to exploit the Coriolis force effect, most micromachined gyroscopes are configured as vibrating gyroscopes since such a configuration avoids the use of rotating parts.
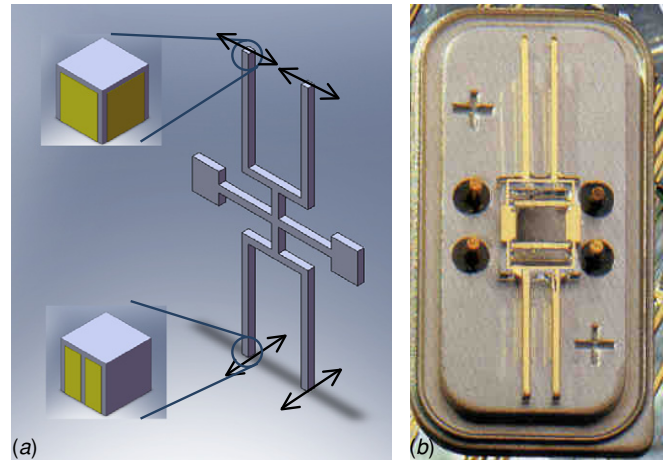
Piezoelectric effect is a natural choice for gyroscopes since it provides a direct method for both the drive, i.e. inducing vibrations, and sensing of the forces, i.e. motion arising as a consequence of Coriolis forces acting on the vibrating parts, due to rate of rotation of objects. Figure 21(a) shows a typical tuning fork gyro design used by Systron Donner division of BEI Technologies made out of a *z*-cut quartz crystal [208–210] and figure 21(b) shows a photograph of the device. It consists of a drive tuning fork which is vibrated in the plane of the device and is coupled to another similar sense tuning fork through a frame. The frame is designed to be able to transmit the torque arising in the drive tines due to the angular rotation of the device about the tine axis to the sense tuning fork. This torque arising due to the rotational rate of the device about the tine axis is oscillatory and causes the sense tuning fork to vibrate out of plane at the same frequency as the drive tines if the two tuning forks are geometrically identical. The sense tines vibrate at an amplitude that is proportional to the angular rate of rotation of the device. This amplitude in turn is picked via piezoelectric effect in quartz by the sense capacitors and using synchronous demodulation and low pass filtering techniques, the sensor output is converted into a dc output [210]. While the principle of operation of the device seems relatively simple, the working of the device is actually determined by the configuration of the electrodes on the drive and sense tines. In the case of quartz, the null value of d_{33} coefficient and the non-zero d_{12} coefficient of quartz which is equal to $-d_{11}$ are used for configuring the drive and sense electrodes on the *z*-cut quartz crystal substrate. A typical Systron Donner quartz rate sensor (QRS) gyroscope has tines that are 500 μm thick, 450 μm wide and 6 mm long and have a resonance frequency of ~10 kHz. A complete description of how the electrodes accomplish these drive and sense functions is described by Senturia [205].

Gyroscopes are specified in terms of resolution, drift, zero rate output and sensitivity or scale factor. The output of the gyro in the absence of any rotation will arise due to thermal white noise in the micromechanical structure and limits the smallest rate of rotation that can be detected. It
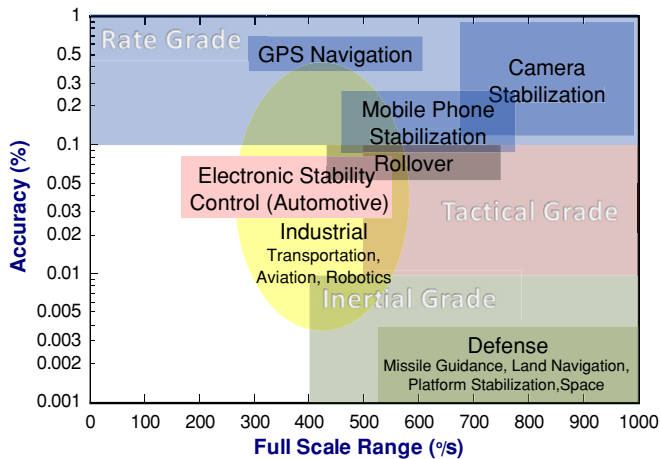
Figure 22. Full scale range and accuracy specification of the various grades of gyros and their typical applications.

can be considered as the noise-equivalent rate of rotation and is typically specified in terms of $(^\circ\ s^{-1})\ Hz^{-1/2}$. The inherently high Q-factor of quartz tuning fork resonators enables a very low limit to this noise in these type of gyros. The sensitivity or the scale factor is a measure of the dc output of the gyroscope per unit rate of rotation. The ratio of the sensitivity to zero rate output is the resolution of the gyroscope. Based on these specifications, gyros can be classified into rate, tactical and inertial grade. Figure 22 shows the typical ranges and accuracies desired for the various applications of gyroscopes. Gyros and accelerometers are being increasingly employed in the automotive industry where electronic stability control is implemented by correcting the deviations between the intended and the measured (actual) course of the vehicle through the use of controlled feedback to the front brakes. In 2007, this market was estimated to be \$837 million for gyros alone of which 37% was captured by Systron Donner's quartz rate sensor [211]. Although silicon micromachined gyros are rapidly gaining ground in the price competitive rate grade automotive gyros market, the tactical and inertial markets are currently dominated by the high performance quartz rate sensors and ring laser gyros [212].

6.6. Piezoelectric micromachined ultrasonic transducers

Piezoelectric thin films can be integrated into freestanding micromechanical structures to create high pixel density arrays of ultrasonic transmitters and receivers also known as piezoelectric micromachined ultrasonic transducers (pMUTs). Piezoelectric transduction allows for the pixels to act as effective emitters as well as receivers of ultrasound. Potential applications of such arrays include handheld diver's sonar, medical ultrasound imaging and nondestructive testing (NDT). Micromachined audio-frequency condenser hydrophones with on-chip JFET buffer amplifiers have also been demonstrated [213]. Micromachined ultrasonic transducers (MUTs) are especially finding increasing applications in medical ultrasonic imaging in the area of intravascular ultrasound imaging (IVUS) where miniaturized high-frequency (3–50 MHz) piezoelectric transducer arrays mounted at the catheter tip can be used for

two- and three-dimensional ultrasound imaging of the vascular system [214]. Using ultrasound transducers of appropriate frequency, any region of the vascular system can be imaged intraluminally using a catheter system. Images are generated from ultrasound waves that are reflected from the vessel walls. Frequencies in the 3–5 MHz are typically used for deep organ investigations whereas frequencies in the 50 MHz region allow for investigations of thin tissues, artery walls, etc [215]. At present, commercial 2D ultrasonic transducer probes are limited to linear arrays with an element pitch of approximately 300 μm and operating frequencies of less than 5 MHz [213]. To produce 2D arrays that operate in the frequency range of 10–15 MHz, which is desirable for real-time 3D intravascular imaging, element pitch on the order of 100 μm or less (less than the acoustic wavelength in tissue) is necessary to suppress grating lobes. pMUTs can be operated in either a pulse-echo mode or a continuous wave mode. In the pulse-echo mode a wave packet of short duration is first emitted and the reflected ultrasound wave packet is received by the same transducer array and analyzed in terms of the amplitude and delay times. In the continuous wave mode the frequency shifts that arise out of a moving boundary due to the Doppler effect are monitored in a narrow frequency band [216].

Popular configurations of pMUTs are either circular ring [217], circular plate or rectangular thin film plates [218]. A pMUT typically consists of a clamped membrane made out of passive material such as SiO_2, Si_3N_4, etc, with a layer of piezoelectric thin film laminated on it. The generation of the ultrasound is accomplished by the flexural motion of the membrane while the transduction of the acoustic wave uses transverse piezoelectric effect. Thin film pMUTs using AlN [219], ZnO [217] and PZT [218] have been reported. Amongst these PZT remains the material of choice due to high coupling coefficients, high piezoelectric constants and superior dielectric constant [220]. Even larger piezoelectric coefficients and electromechanical coupling coefficients can be obtained by using relaxor ferroelectric crystals such as PMN–PT. The piezoelectric strain in these materials remains nearly hysteresis free up to levels of ~0.5–0.6% depending on the crystal composition [102]. Bulk micromachined PMN–PT transducers can be configured to exploit the much higher electromechanical coupling coefficient (k_{33}) and figure of merit $(d_{33} \times g_{33})$ of single crystal piezoelectrics for ultrasound transducer applications [102, 104, 221]. Acoustic impedance matching is another important design consideration which determines what materials to layer with the pMUT. 2D array pixel density and size determine the directivity and side-lobe patterns of the ultrasound waves. Figure 23 shows the calculated directivity pattern of ultrasonic waves in air as a function of aperture size and array density [222]. Clearly high density arrays result in small side lobes (figure 23(*c*)) whereas large aperture results in greater directivity (figure 23(*b*)). For further details, the interested reader is directed to dedicated reviews of pMUTs [16, 220].

7. Concluding remarks

As we have seen through this review, the field of piezoelectric MEMS sensors is a rapidly evolving area of research and
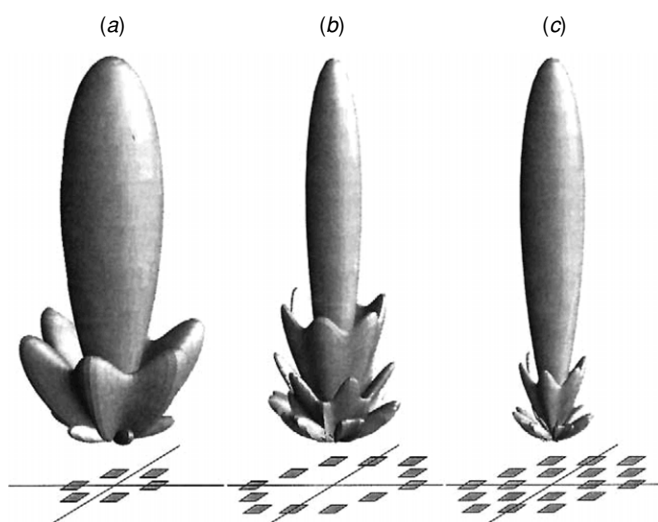
Figure 23. Calculated directivity of ring arrays of ultrasonic transducers for applications in air taken from Yamashita *et al* [223]. (*a*) Six-element small array (ultrasound wavelength determines the directivity pattern of the sensor array when the elements are arranged regularly at equal spacing), (*b*) 12-element large array and (*c*) 18-element dense array. Sharpness of the directivity is almost proportional to the ratio of the size of array to the wavelength, and large spacing between adjacent elements makes large side lobes when the wavelength is fixed.

development with several micromachined devices having been successfully commercialized at this time. The motivation to miniaturize sensors primarily arises from the requirement that the best sensors need to be designed to exchange minimal amount of energy with the measurand since this ensures minimal perturbation in measurements. Piezoelectric materials, especially in thin film form, can be incorporated into micromachined sensor structures making it possible to achieve high signal to noise ratios. Additive, subtractive and integrative fabrication processes can be used to realize piezoelectric MEMS devices.

At present, piezoelectric materials such as quartz, langasite, lithium niobate and lithium tantalate are only available as bulk single crystals and can be configured as high-performance transducers through direct bulk micromachining or hybrid integration methods. These materials exhibit very high material Q-factors and are typically configured as acoustic wave resonators. For example, the exceptional temperature stability and extremely low phase noise of quartz resonators have continued this material's dominance as the de facto frequency standard material in the electronics and wireless communication areas. Only recently sputtering methods in the 200–500 °C temperature range have been developed for the deposition of high quality AlN films. The high degree of control over the textured columnar growth thin films of AlN, with the *c*-axis oriented perpendicular to the substrate and extremely low dielectric loss, has already spurred the successful commercialization of AlN FBARs from Agilent Technologies. Another significant material that is readily available in thin film form is the ferroelectric lead zirconate titanate. PZT films at the morphotropic phase boundary with a Zr/Ti ratio of 52/48 have been shown to exhibit a maximum

in the piezoelectric response and are typically used in MEMS, microactuator and microsensor applications. PZT films are typically deposited using the sol–gel (chemical solution) process which enables uniform deposition of high quality films with well-controlled compositions on large diameter substrates at low cost. Recent advances in templated and textured growth of piezoelectric thin films have enabled achievement of piezoelectric coefficients in thin films that approach the values of their bulk counterparts.

Most piezoelectric materials can be patterned via wet or dry etching processes. Wet etching techniques, while relatively simple, can detrimentally affect the piezoelectric properties as well as other masking and/or electrically active materials/layers in the device structure. Dry etching techniques based on the use of reactive plasmas offer an attractive alternative to the wet patterning techniques for piezoelectrics. The main consideration in the choice of gas species for plasma etching depends upon the formation of volatile products as part of the breakdown of the metal (semiconductor) oxides being etched. Since the fluorides and chlorides of most transition metals and metal oxides are non-volatile compounds, the reactive component of etching is typically an insignificant part of the etching process, and thus relies on the physical sputtering of the surface atoms due to the bombardment of energetic ions. Therefore, most of piezoelectric etching recipes use inert gases as part of the etch gas composition as the sputter yield of inert gases is much higher than other elements/molecules. The availability of reliable, high throughput, high aspect ratio micromachining processes has now created new opportunities for realizing novel MEMS devices from bulk piezoelectric materials such as quartz, lithium tantalate, aluminum nitride, PZT and single crystal PMN–PT.

In spite of several materials' deposition, processing, patterning and integration challenges, a number of piezoelectric devices have been successfully commercialized. These include (i) AlN-nitride-based FBARs from Agilent Technologies, (ii) quartz rate sensor from BEI Technologies and (iii) BST- and PZLT-based room temperature focal plane IR sensor arrays from Texas Instruments. However, looking into the future, several challenges currently remain. While chemical solution methods offer attractive low cost methods for the deposition of uniform films of piezoelectrics, the success of these methods is still predicated upon the use of appropriate layers for proper nucleation and film growth. As a consequence, the sensor structure often consists of multi-layered material stacks and requires extensive device-specific development efforts. Further understanding of thin film piezoelectric materials is also required to reduce and control material and sensor drift and aging characteristics. Optimization of the residual stress in individual layers to result in an overall stress-compensated sensor structure continues to pose a significant challenge. Material deposition techniques in thin film form with properties approaching those of bulk materials are another area of significant challenges. While this has been successfully demonstrated for PZT thin films, the concepts are being currently broadened to produce relaxor ferroelectric films. Chemistries and etching characteristics of

these materials still remain slow with the fastest rates being $\sim 20\,\mu\text{m h}^{-1}$ for PZT films, and further improvements are still desired.

From piezoelectric device perspective, recent work on micromachined, high-frequency, bulk acoustic wave resonators has allowed for the investigation of atomically thin layers of viscoelastic materials in a fluid ambient. Real-time investigation of such a phenomenon can be the basis of next generation biosensors. Based on fluid-surface acoustic wave interaction, an acoustic streaming phenomenon has been demonstrated and can be utilized for micro-transport of the molecules and nanoparticles on sensor surfaces. Recent experimental work has shown that the Rayleigh waves produced in lithium niobate and in lithium tantalate can be effectively used to clean the sensor surface through the use of acoustic streaming using Rayleigh waves, and such concepts will be likely incorporated into the next generation biochemical sensors. Another area of application for piezoelectric materials is micromachined ultrasonic transducer (MUT) arrays. pMUTs are especially finding increasing applications in medical ultrasonic imaging, especially in the area of IVUS where miniaturized high-frequency (3–50 MHz) piezoelectric transducer arrays mounted at the catheter tip can be used for two- and three-dimensional ultrasound imaging of the vascular system. In the area of inertial systems, piezoelectric devices are expected to dominate the markets especially for tactical and inertial grade devices, due to their superior performance. In summary, as piezoelectric materials technology, fabrication processes and modeling/design tool sets improve, the next generations of micromachined piezoelectric sensors have the potential of operating at or near the fundamental thermal fluctuation limits.

Acknowledgments

References

[1] Setter N *et al* 2006 Ferroelectric thin films: review of materials, properties, and applications *J. Appl. Phys.* **100** 051606

[2] Muralt P 2000 Ferroelectric thin films for micro-sensors and actuators: a review *J. Micromech. Microeng.* **10** 136–46

[3] Trolier-McKinstry S and Muralt P 2004 Thin film piezoelectrics for MEMS *J. Electroceram.* **12** 7–17

[4] Ruby R 2007 Review and comparison of bulk acoustic wave FBAR, SMR technology *Proc. IEEE Ultrasonics Symp.* vol 7 pp 1029–40

[5] http://www.systron.com/

[6] DeVoe D L and Pisano A P 2001 Surface micromachined piezoelectric accelerometers (PiXLs) *J. Microelectromech. Syst.* **10** 180–6

[7] Vellekoop M J *et al* 1990 Compatibility of zinc oxide with silicon IC processing *Sensors Actuators* A **23** 1027–30

[8] Mancini R 2002 *Op Amps for Everyone: Design Reference* vol SLOD006B ed R Mancini (Dallas: Texas Instruments)

[9] Ikeda T 1990 *Fundamentals of Piezoelectricity* (New York: Oxford University Press) p 9

[10] Schwartz R W, Ballato J and Haertling G H 2004 Piezoelectric and electro-optic ceramics *Ceramic Materials for Electronics* ed R C Buchanan (New York: Dekker) pp 207–315

[11] Xu Y 1991 *Ferroelectric Materials and their Applications* (Amsterdam: North-Holland) pp 61–3, 226–9

[12] Cady W G 1946 *Piezoelectricity* (New York: McGraw-Hill)

[13] Setter N 2005 Electroceramics-based MEMS: fabrication-technology, and applications *Electronic Materials: Science and Technology* ed H L Tuller (New York: Springer)

[14] Uchino K 2000 *Ferroelectric Devices* (New York: Dekker)

[15] Muralt P 2006 Texture control and seeded nucleation of nanosize structures of ferroelectric thin films *J. Appl. Phys.* **100** 051605

[16] Muralt P *et al* 2005 Piezoelectric micromachined ultrasonic transducers based on PZT thin films *IEEE Trans. Ultrason. Ferroelectr. Freq. Control* **52** 2276–88

[17] Setter N 2002 ABC of piezoelectric materials *Piezoelectric Materials in Devices* ed N Setter (Lausanne: Ceramics Laboratory, EPFL Swiss Federal Institute of Technology) pp 1–28

[18] Naik R S *et al* 1999 Low-temperature deposition of highly textured aluminum nitride by direct current magnetron sputtering for applications in thin-film resonators *J. Electrochem. Soc.* **146** 691–6

[19] Dubois M A and Muralt P 1999 Properties of aluminum nitride thin films for piezoelectric transducers and microwave filter applications *Appl. Phys. Lett.* **74** 3032–4

[20] Bottom V E 1982 *Introduction to Quartz Crystal Unit Design* (New York: Van Nostrand-Reinhold) p 4

[21] Goyal A, Zhang Y and Tadigadapa S 2005 *Y*-cut quartz resonator based calorimetric sensor *Proc. IEEE Sensors Conf.* pp 1241–4

[22] Rabe J *et al* 2003 Monolithic miniaturized quartz microbalance array and its application to chemical sensor systems for liquids *Sensors J. IEEE* **3** 361–8

[23] Goyal A, Joshi P, Gupta A, Eklund P and Tadigadapa S 2005 Micromachined quartz resonator functionalized with single walled carbon nanotubes *Proc. IEEE Sensors Conf.* pp 841–4

[24] Nakamura T 2007 Growth of quartz thin films by catalyst-enhanced vapour-phase epitaxy under atmospheric pressure *Proc. IEEE Int. Freq. Control Symp.* pp 1064–6

[25] Zhang H *et al* 2002 Liquid phase epitaxy growth of langasite film for resonators and oscillators *J. Cryst. Growth* **234** 660–5

[26] Liufu D and Kao K C 1998 Piezoelectric, dielectric, and interfacial properties of aluminum nitride films *J. Vac. Sci. Technol.* A **16** 2360–6

[27] Wang L-P, Ginsburg E, Gerfers F, Samara-Rubio D, Weinfeld B, Qing M, Rao V and He M Y 2006 Sputtered AlN thin films for piezoelectric MEMS devices *Proc. IEEE Sensors Conf.* pp 10–13

[28] Tonisch K *et al* 2006 Piezoelectric properties of polycrystalline AlN thin films for MEMS application *Sensors Actuators* A **132** 658–63

[29] Tabbal M *et al* 2001 Pulsed laser deposition of c-axis oriented aluminum nitride thin films on silicon *Eur. Phys. J. Appl. Phys.* **14** 115–9

[30] Alexander T P, Bukowski T J, Uhlmann D R, Teowee G, McCarthy K C, Dawley J and Zelinski B J J 1996 Dielectric properties of sol-gel derived ZnO thin films

Proc. 10th IEEE Int. Symp. on Applications of Ferroelectrics (ISAF '96) vol 2, pp 585–8

[31] Molarius J, Kaitila J, Pensala T and Ylilammi M 2003 Piezoelectric ZnO films by r.f. sputtering *J. Mater. Sci.: Mater. Electron.* **14** 431–5

[32] Dang W L *et al* 2007 Deposition and characterization of sputtered ZnO films *Superlattices Microstruct.* **42** 89–93

[33] Villanueva Y Y, Liu D-R and Cheng P T 2006 Pulsed laser deposition of zinc oxide *Thin Solid Films* **501** 366–9

[34] Xu F, Wolf R A, Yoshimura T and Trolier-McKinstry S 2002 Piezoelectric films for MEMS applications *Proc. 11th Int. Symp. on Electrets* pp 386–96

[35] Es-Souni M *et al* 2005 Pyroelectric and piezoelectric properties of thick PZT films produced by a new sol-gel route *J. Eur. Ceram. Soc.* **25** 2499–503

[36] Gentil S, Kohli M and Seifert A 2007 PZT thick films by Diol chemical solution deposition *J. Electroceram.* **19** 307–10

[37] Wang Z J *et al* 2004 Preparation and characterization of PZT thin films deposited by pulsed laser deposition on template layer *J. Eur. Ceram. Soc.* **24** 1629–32

[38] Muralt P 2008 Recent progress in materials issues for piezoelectric MEMS *J. Am. Ceram. Soc.* **91** 1385–96

[39] Grudkowski T W *et al* 1980 Fundamental-mode VHF/UHF miniature acoustic resonators and filters on silicon *Appl. Phys. Lett.* **37** 993–5

[40] Lakin K M, Wang J S, Kline G R, Landin A R, Chen Y Y and Hunt J D 1982 Thin film resonators and filters *Proc. IEEE Ultrasonics Symp.* pp 466–75

[41] Zhou B, Wang J, Pan Y, Wang L and Peng H 2008 Fabrication and physical properties of high-quality zinc oxide thin films *Proc. SPIE* **6984** 69840S

[42] Jiang H X, Ugolini C, Lin J Y and Zavada J M 2006 III-nitride wide bandgap semiconductors for optical communications *19th Annual Meeting of the IEEE Lasers and Electro-Optics Society* pp 36–7

[43] Ballato A and Gualtieri J G 1994 Advances in high-Q piezoelectric resonator materials and devices *IEEE Trans. Ultrason. Ferroelectr. Freq. Control* **41** 834–44

[44] Ssakharov S A, Larionov I M and Medvedev A V 1992 Application of langasite crystals in monolithic filters operating in shear modes *Proc. 46th IEEE Frequency Control Symp.* pp 713–23

[45] Kovacs G, Anhorn M, Engan H E, Visintini G and Ruppel C C W 1990 Improved material constants for LiNbO$_3$ and LiTaO$_3$ *Proc. IEEE Ultrasonics Symp.* vol 1, pp 435–8

[46] Ilyaev A B *et al* 1986 Temperature dependence of electromechanical properties of LGS crystals *Phys. Status Solidi* **98** 5

[47] Carr P H and O'Connell R M 1979 New method for determining temperature coefficients of bare piezoelectrics *Proc. IEEE Ultrasonics Symp.* pp 595–7

[48] Sliker T R and Koneval D J 1968 Frequency-temperature behavior of X-cut lithium tantalate resonators *Proc. IEEE* **56** 1402

[49] Ledermann N *et al* 2003 {1 0 0}-Textured, piezoelectric Pb(Zr$_x$, Ti$_{1-x}$)O$_3$ thin films for MEMS: integration, deposition and properties *Sensors Actuators* A **105** 162–70

[50] Trolier-McKinstry S and Muralt P 2005 *Electroceramic-Based MEMS* ed N Setter (New York: Springer) pp 199–215

[51] Chang C, Wang J, Lin C and Chen K 2000 The fabrication and characterization of PZT thin film acoustic devices for application in underwater robotic systems *Proc. National Science Council (Republic of China)* **24** 287–92

[52] Wang L-P 2001 Microelectromechanical systems (MEMS) sensors based on lead zirconate titanate (PZT) films *PhD Thesis* Pennsylvania State University

[53] Frantti J, Moilanen H, Leppavouri S and Uusimaki A 1993 Laser ablation of PZT films for use in bimorph actuator structures *Proc. Mater. Res. Soc. Symp.* **285** 415

[54] Pandey S K *et al* 2004 Electrical properties of PZT thin films grown by sol-gel and PLD using a seed layer *Mater. Sci. Eng.* B **112** 96–100

[55] Dorey R A and Whatmore R W 2005 Ceramic thick films for MEMS *Electroceramic-Based MEMS: Fabrication-Technology and Applications* ed N Setter (New York: Springer) pp 177–97

[56] Wolf R A 2001 Temperature dependence of the piezoelectric response of lead zirconate titanate films for MEMS applications *PhD Thesis* Pennsylvania State University

[57] Hong E 2004 Surface micromachined peristaltic pumps using lead zirconate titanate film *PhD Thesis* Pennsylvania State University

[58] Seung-Eek P and Shrout T R 1997 Characteristics of relaxor-based piezoelectric single crystals for ultrasonic transducers *IEEE Trans. Ultrason. Ferroelectr. Freq. Control* **44** 1140–7

[59] Srinivasan P and Spearing S M 2008 Optimal materials selection for bimaterial piezoelectric microactuators *J. Microelectromech. Syst.* **17** 462–72

[60] Zhang S *et al* 2002 Dielectric and piezoelectric properties of high Curie temperature single crystals in the PYN-PT solid solution series *Japan. J. Appl. Phys.* **41** 722–6

[61] Deleuze M, Cambon O, Goiffon A, Ibanez A and Philippot E 1993 Controlled dissolution applied to berlinite and quartz materials *Proc. IEEE 47th Int. Frequency Control Symp.* pp 381–9

[62] Vig J R, Lebus J W and Filler R L 1977 Chemically polished quartz *Proc. IEEE 31st Annual Symp. on Frequency Control* pp 131–43

[63] Vondeling J K 1983 Fluoride-based etchants for quartz *J. Mater. Sci.* **18** 304–14

[64] Danel J S and Delapierre G 1991 Quartz: a material for microdevices *J. Micromech. Microeng.* **1** 187–98

[65] Sheng T Y, Yu Z Q and Collins G J 1988 Disk hydrogen plasma assisted chemical vapor deposition of aluminum nitride *Appl. Phys. Lett.* **52** 576–8

[66] Dubois M A, Muralt P and Plessky V 1999 BAW resonators based on aluminum nitride thin films *Proc. IEEE Ultrasonics Symp.* pp 907–10

[67] Huang L *et al* 1996 Chemical etching of ion beam deposited AlN and AlN:H *Thin Solid Films* **279** 43–8

[68] Vartuli C B *et al* 1996 Wet chemical etching of AlN and InAlN in KOH solutions *J. Electrochem. Soc.* **143** 3681–4

[69] Bickermann M *et al* 2007 Wet KOH etching of freestanding AlN single crystals *J. Cryst. Growth* **300** 299–307

[70] Pearton S J *et al* 2004 Recent advances in processing of ZnO *J. Vac. Sci. Technol.* B **22** 932–48

[71] Li Y, Tompa G S, Liang S, Gorla C, Lu Y and Doyle J 1997 Transparent and conductive Ga-doped ZnO films grown by low pressure metal organic chemical vapor deposition *Proc. 43rd National Symp. of the American Vacuum Society* vol 15, pp 1063–8

[72] Beeby S P, Blackburn A and White N M 1999 Processing of PZT piezoelectric thick films on silicon for microelectromechancial systems *J. Micromech. Microeng.* **9** 218–29

[73] Wang L-P, Wolf R, Zhou Q, Trolier-McKinstry S and Davis R J 2001 Wet-etch patterning of lead zirconate titanate (PZT) thick films for microelectromechanical systems (MEMS) applications *Proc. Mater. Res. Soc. Symp.* pp EE5.39.1–6

[74] Zheng K, Jian L and Jiaru C 2003 Study on wet-etching of PZT thin film *Proc. Int. Microprocesses and Nanotechnology Conf.* pp 248–9

26

[75] Gross S J, Zhang Q, Tadigadapa S, Trolier-McKinstry S, Jackson T N and Djuth F T 2001 Reliable integration of piezoelectric lead zirconate titanate with MEMS fabrication processes *Proc. SPIE* **4558** 72–80

[76] Steinbruchel C 1983 Langmuir probe measurements on CHF_3 and CF_4 plasmas: the role of ions in the reactive sputter etching of SiO_2 and Si *J. Electrochem. Soc.* **130** 648–55

[77] Zhuang D and Edgar J H 2005 Wet etching of GaN, AlN, and SiC: a review *Mater. Sci. Eng.* R **48** 1–46

[78] Gardeniers J G E, Rittersma Z M and Burger G J 1998 Preferred orientation and piezoelectricity in sputtered ZnO films *J. Appl. Phys.* **83** 7844–54

[79] Trolier S, Gelst C, Safari A, Newnham R E and Xu Q C 1986 Etched piezoelectric structures *Proc. 6th IEEE Int. Symp. on Applications of Ferroelectrics* pp 707–10

[80] Leech P W 1998 Reactive ion etching of piezoelectric materials in CF4/CHF3 plasmas *J. Vac. Sci. Technol.* A **16** 2037–41

[81] Campbell S A 2001 *The Science and Engineering of Microelectronic Fabrication* 2nd edn (New York: Oxford University Press)

[82] Li L, Abe T and Esashi M 2003 Smooth surface glass etching by deep reactive ion etching with SF_6 and Xe gases *J. Vac. Sci. Technol.* B **21** 2545

[83] Subasinghe S S, Goyal A and Tadigadapa S 2006 High aspect ratio plasma etching of bulk lead zirconate titanate *Proc. SPIE* **6109** 100–8

[84] Khan F A *et al* 2002 High rate etching of AlN using BCl3/Cl2/Ar inductively coupled plasma *Mater. Sci. Eng.* B **95** 51–4

[85] Engelmark F, Iriarte G F and Katardjiev I V 2002 Selective etching of Al/AlN structures for metallization of surface acoustic wave devices *J. Vac. Sci. Technol.* B **20** 843–8

[86] Shul R J *et al* 1998 Selective inductively coupled plasma etching of group-III nitrides in Cl2- and BCl3-based plasmas *J. Vac. Sci. Technol.* A **16** 621

[87] Woo J C *et al* 2008 Etching characteristic of ZnO thin films in an inductively coupled plasma *Surf. Coat. Technol.* **202** 5705–8

[88] Bale M and Palmer R E 2001 Deep plasma etching of piezoelectric PZT with SF_6 *J. Vac. Sci. Technol.* B **19** 2020–5

[89] Schreiter S and Poll H U 1992 A new plasma-etching technique for micromechanical structuring of quartz *Sensors Actuators* A **35** 137–41

[90] Goyal A, Hood V and Tadigadapa S 2006 High speed anisotropic etching of Pyrex(R) for microsystems applications *J. Non-Cryst. Solids* **352** 657

[91] Smith S A *et al* 1997 High rate and selective etching of GaN, AlGaN, and AlN using an inductively coupled plasma *Appl. Phys. Lett.* **71** 3631–3

[92] Mastropaolo E *et al* 2007 Reactive ion etching of zinc oxide (ZnO) in SiCl4 based plasmas *Electron. Lett.* **43** 1467–9

[93] Lim W T *et al* 2007 Comparison of plasma chemistries for the dry etching of bulk single-crystal zinc-oxide and rf-sputtered indium-zinc-oxide films *Appl. Surf. Sci.* **253** 9228–33

[94] Lim W *et al* 2006 Comparison of ZnO dry etching in high density inductively coupled CH_4/H_2 and C_2H_6/H_2-based chemistries *ECS Trans.* **2** (5) 209–16

[95] Efremov A M *et al* 2004 Etching characteristics and mechanism of Pb(Zr,Ti)O3 thin films in CF4/Ar inductively coupled plasma *Vacuum* **75** 321–9

[96] Smith J H and Senturia S D 1995 Self-consistent temperature compensation for resonant sensors with application to quartz bulk acoustic wave chemical sensors *8th Int. Conf.*

[97] Rabe J, Seidemann V and Buettgenbach S 2003 Monolithic fabrication of wireless miniaturized quartz crystal microbalance (QCM-R) array for biochemical sensing *12th Int. Conf. on Solid-State Sensors, Actuators and Microsystems, Transducers 03* pp 1875–8

[98] Lin Z *et al* 1993 Operation of an ultrasensitive 30-MHz quartz crystal microbalance in liquids *Anal. Chem.* **65** 1546–51

[99] Vu Ngoc H *et al* 2003 High-frequency one-chip multichannel quartz crystal microbalance fabricated by deep RIE *Sensors Actuators* A **108** 91

[100] Goyal A, Tadigadapa S, Gupta A and Eklund P C 2005 Use of single-walled carbon nanotubes to increase the quality factor of an *AT*-cut micromachined quartz resonator *Appl. Phys. Lett.* **87** 204102

[101] Kao P *et al* 2008 Human serum albumin adsorption study on 62-MHz miniaturized quartz gravimetric sensors *Anal. Chem.* **80** 5930–6

[102] Jiang X, Snook K, Hackenberger W S and Geng X 2007 Single crystal piezoelectric composites for advanced NDT ultrasound *Proc. SPIE* **6531** 65310F

[103] Yuan J R, Jiang X, Cao P-J, Sadaka A, Bautista R, Snook K and Rehrig P W 2006 High frequency piezo composites microfabricated ultrasound transducers for intravascular imaging *Proc. IEEE Ultrasonics Symp.* pp 264–8

[104] Jiang X, Snook K, Walker T, Portune A, Haber R, Geng X, Welter J and Hackenberger W S 2008 Single crystal piezoelectric composite transducers for ultrasound NDE applications *Proc. SPIE* **6934** 69340D

[105] Kommepalli H, Hirsh A, Tadigadapa S and Rahn C 2008 Piezoelectric T-beam microactuators *Proc. ASME 2008 Int. Design Engineering Technical Conf. and Computers and Information in Engineering Conf. (IDETC/CIE) (New York)*

[106] Stoffel A, Kovacs A, Kronast W and Muller B 1996 LPCVD against PECVD for micromechanical applications *J. Micromech. Microeng.* **6** 1–13

[107] Bustillo J M, Howe R T and Muller R S 1998 Surface micromachining for microelectromechanical systems *Proc. IEEE* **86** 1552–74

[108] Gross S J 2004 Micromachined switches and cantilever actuators based on piezoelectric lead zirconate titanate (PZT) *PhD Thesis* Pennsylvania State University

[109] Hannink R H J, Kelly P M and Muddle B C 2000 Transformation toughening in zirconia-containing ceramics *J. Am. Ceram. Soc.* **83** 461–87

[110] Brenier R 2002 Stress and moisture-sorption in ozone-annealed films of zirconium oxide obtained from sol-gel *J. Sol-Gel Sci. Technol.* **25** 57–63

[111] Polcawich R 2007 Design, fabrication, test and evaluation of RF MEMS series switches using lead zirconate titanate (PZT) thin film actuators *PhD Thesis* Pennsylvania State University

[112] Tabata O *et al* 1989 Mechanical property measurements of thin films using load-deflection of composite rectangular membranes *Sensors Actuators* **20** 135–41

[113] Chang F I, Yeh R, Lin G, Chu P B, Hoffman E, Kruglick E J J, Pister K S J and Hecht M H 1995 Gas-phase silicon micromachining with xenon difluoride *Proc. SPIE* **2641** 117–28

[114] Williams K R and Muller R S 1996 Etch rates for micromachining processing *J. Microelectromech. Syst.* **5** 256–69

[115] Goyal A, Tadigadapa S and Islam R 2003 Solder bonding for microelectricalmechanical systems (MEMS) applications *Proc. SPIE* **4980** 281–8

on Solid-State Sensors and Actuators and Eurosensors IX. Transducers '95 pp 724–7

27

[116] Goyal A, Cheong J and Tadigadapa S 2004 Tin-based solder bonding for MEMS fabrication and packaging applications *J. Micromech. Microeng.* **14** 819–25

[117] Cheong J, Goyal A, Tadigadapa S and Rahn C 2003 Reliable bonding using indium based solders *Proc. SPIE* **5343** 114–20

[118] Cheong J, Tadigadapa S and Rahn C 2005 Fabrication and performance of a flextensional microactuator *J. Micromech. Microeng.* **15** 1947–55

[119] Hanson C M 1993 Uncooled thermal imaging at Texas Instruments *Proc. SPIE* **2020** 330–9

[120] Bi F Z and Barber B P 2008 Bulk acoustic wave RF technology *IEEE Microwave Magazine* **8** 65–80

[121] Krishnaswamy S V *et al* 1991 Compact FBAR filters offer low-loss performance *Microw. RF* **30** 127–36

[122] Lakin K M, Kline G R and McCarron K T 1993 High-Q microwave acoustic resonators and filters *IEEE Trans. Microw. Theory Tech.* **41** 2139–46

[123] Shockley W, Curran D R and Koneval D J 1967 Trapped-energy modes in quartz filter crystals *J. Acoust. Soc. Am.* **41** 981–93

[124] Rosenbaum J F 1988 *Bulk Acoustic Wave Theory and Devices* (Boston: Artech House Publishers)

[125] Chandrahalim H *et al* 2008 Performance comparison of Pb(Zr$_{0.52}$Ti$_{0.48}$)O$_3$-only and Pb(Zr$_{0.52}$Ti$_{0.48}$)O$_3$-on-silicon resonators *Appl. Phys. Lett.* **93** 233504

[126] Lakin K M 1999 Thin film resonators and filters *Proc. IEEE Ultrasonics Symp.* pp 895–906

[127] Dubois M A, Muralt P, Matsumoto H and Plessky V 1998 Solidly mounted resonator based on aluminum nitride thin film *Proc. IEEE Ultrasonics Symp.* pp 909–12

[128] Xu F, Trolier-McKinstry S, Ren W and Xu B 2001 Domain wall motion and its contribution to the dielectric and piezoelectric properties of lead zirconate titanate films *J. Appl. Phys.* **89** 1336–48

[129] Nam K *et al* 2008 Monolithic 1-chip FBAR duplexer for W-CDMA handsets *Sensors Actuators* A **143** 162–8

[130] Walls F L and Vig J R 1995 Fundamental limits on the frequency stabilities of crystal oscillators *IEEE Trans. Ultrason. Ferroelectr. Freq. Control* **42** 576–89

[131] Bandey H L *et al* 1999 Modeling the responses of thickness-shear mode resonators under various loading conditions *Anal. Chem.* **71** 2205–14

[132] Lucklum R and Hauptmann P 2000 The quartz crystal microbalance: mass sensitivity, viscoelasticity and acoustic amplification *Sensors Actuators* B **70** 30–6

[133] Rodahl M and Kasemo B 1996 On the measurement of thin liquid overlayers with the quartz-crystal microbalance *Sensors Actuators* A **54** 448–56

[134] Voinova M V, Rodahl M, Jonson M and Kasemo B 1999 Viscoelastic acoustic response of layered polymer films at fluid-solid interfaces: continuum mechanics approach *Phys. Scr.* **59** 391

[135] Mecea V and Bucur R V 1979 The mechanism of the interaction of thin films with resonating quartz crystal substrates: the energy transfer model *Thin Solid Films* **60** 73–84

[136] Sauerbrey G 1959 Verwendung von Schwingquarzen zur Wagung dunner Schichten und zur Mikrowagung *Z. Phys.* **155** 206–22

[137] Vig J R, Filler R L and Kim Y 1996 Uncooled IR imaging array based on quartz microresonators *J. Microelectromech. Syst.* **5** 131–7

[138] Kanazawa K K and Gordon J G 1985 Frequency of a quartz microbalance in contact with liquid *Anal. Chem.* **57** 1770–1

[139] Rodriguez-Pardo L, Farina J, Gabrielli C, Perrot H and Brendel R 2004 Resolution in quartz crystal oscillator circuits for high sensitivity microbalance sensors in damping media *Sensors Actuators* B **103** 318–24

[140] Janshoff A, Galla H-J and Steinem C 2000 Piezoelectric mass sensing devices as biosensors—an alternative to optical biosensors? *Angew. Chem., Int. Ed.* **39** 4004–32

[141] Ferrari V *et al* 2000 Multisensor array of mass microbalances for chemical detection based on resonant piezo-layers of screen-printed PZT *Sensors Actuators* B **68** 81–7

[142] Michalzik M *et al* 2005 Development and application of a miniaturised quartz crystal microbalance (QCM) as immunosensor for bone morphogenetic protein-2 *Sensors Actuators* B **105** 508

[143] Kao P, Doerner S, Schneider T, Allara D, Hauptmann P and Tadigadapa S 2009 A micromachined quartz resonator array for biosensing applications *J. Microelectromech. Syst.* **18** 522–30

[144] Kao P, Allara D and Tadigadapa S 2009 Characterization of viscoelastic properties of adsorbed biomolecules and biomolecular assemblies with high frequency micromachined quartz resonators *Sensors Actuators* B available online: doi:10.1016/j.snb.2009.01.046

[145] Kao P, Allara D and Tadigadapa S 2009 Fabrication and performance characteristics of high-frequency micromachined bulk acoustic wave quartz resonator arrays *Meas. Sci. Technol.* at press

[146] Kao P, Strutwolf J, Arrigan D, Allara D and Tadigadapa S 2009 Characterization of diffuse double layer viscoelasticity in electrochemical atom deposition using high frequency micromachined quartz crystal resonators *Langmuir* submitted

[147] Ballantine D S *et al* 1997 *Acoustic Wave Sensors: Theory, Design, and Physico-Chemical Applications. Applications of Modern Acoustics* ed R Stern and M Levy (San Diego, CA: Academic)

[148] Cavic B A, Hayward G L and Thompson M 1999 Acoustic waves and the study of biochemical macromolecules and cells at the sensor-liquid interface *Analyst* **124** 1405–20

[149] Thompson M and Stone D C 1997 *Surface-launched Acoustic Wave Sensors: Chemical Sensing and Thin Film Characterization* (New York: Wiley)

[150] James D *et al* 2005 Chemical sensors for electronic nose systems *Microchim. Acta* **149** 1–17

[151] Hoyt A E *et al* 1998 SAW sensors for the room-temperature measurement of CO$_2$ and relative humidity *Anal. Chem.* **70** 2137–45

[152] Kawalec A and Pasternak M 2008 A new high-frequency surface acoustic wave sensor for humidity measurement *IEEE Trans. Instrum. Meas.* **57** 2019–23

[153] Shen C-Y and Liou S-Y 2008 Surface acoustic wave gas monitor for ppm ammonia detection *Sensors Actuators* B **131** 673–9

[154] Staples E J and Viswanathan S 2008 Detection of contrabands in cargo containers using a high-speed gas chromatograph with surface acoustic wave sensor *Ind. Eng. Chem. Res.* **47** 8361–7

[155] Andrä J, Böhling A, Gronewold T M A, Schlecht U, Perpeet M and Gutsmann T 2008 Surface acoustic wave biosensor as a tool to study the interaction of antimicrobial peptides with phospholipid and lipopolysaccharide model membranes *Langmuir* **24** 9148–53

[156] Chiu C-S *et al* 2008 Immobilization of DNA-Au nanoparticles on aminosilane-functionalized aluminum nitride epitaxial films for surface acoustic wave sensing *Appl. Phys. Lett.* **93** 163106

[157] Wenzel S W and White R M 1989 Analytic comparison of the sensitivities of bulk-wave, surface-wave, and flexural plate-wave ultrasonic gravimetric sensors *Appl. Phys. Lett.* **54** 1976–8

[158] Jakoby B and Vellekoop M 1997 Properties of Love waves: applications in sensors *Smart Mater. Struct.* **6** 668–79

[159] Drafts B 2001 Acoustic wave technology sensors *IEEE Trans. Microw. Theory Tech.* **49** 795–802

[160] Watson G and Staples E 1990 SAW resonators as vapor sensors *Proc. IEEE Ultrasonics Symp.* pp 311–14

[161] Grate J W, Wenzel S W and White R M 1991 Flexural plate wave devices for chemical analysis *Anal. Chem.* **63** 1552–61

[162] Chou F-F and Shih J-S 2008 Electrochemical electrode/SAW system for metal ions and glucose in solutions *Sensors Actuators* B **129** 176–83

[163] Luginbuhl P *et al* 1997 Microfabricated Lamb wave device based on PZT sol-gel thin film for mechanical transport of solid particles and liquids *J. Microelectromech. Syst.* **6** 337–46

[164] Lin H-B and Shih J-S 2003 Fullerene C60-cryptand coated surface acoustic wave quartz crystal sensor for organic vapors *Sensors Actuators* B **92** 243–54

[165] Pestov D *et al* 2007 Improving the stability of surface acoustic wave (SAW) chemical sensor coatings using photopolymerization *Sensors Actuators* B **126** 557–61

[166] Jung J-P *et al* 2004 Fabrication and characterization of high frequency SAW device with IDT/ZnO/AlN/Si configuration: role of AlN buffer *Thin Solid Films* **447–448** 605–9

[167] Cular S *et al* 2005 Removal of nonspecific binding on microsensors using surface acoustic waves *AIChE Annual Meeting (Cincinnati, OH)*

[168] Cular S *et al* 2008 Removal of nonspecific binding on microsensors using surface acoustic waves *IEEE Sensors J.* **8** 314–20

[169] Cular S *et al* 2005 Acoustic manipulation of biological samples for improved sensors *AIChE Annual Meeting, Conf. Proc. (Cincinnati, OH)*

[170] Kruse P W 1995 Uncooled IR focal plane arrays *Proc. SPIE* **2552** 556–63

[171] Tadigadapa S and Zhang Y 2006 *Encyclopedia of Sensors* ed E D C Grimes and M Pishko (Valencia, CA: American Scientific Publishers) vol 10, pp 247–77

[172] Wood R A 1993 Uncooled thermal imaging with monolithic silicon focal planes *Proc. SPIE* **2020** 322–9

[173] Rogalski A 2003 Infrared detectors: status and trends *Prog. Quantum Electron.* **27** 59

[174] Bogue R 2007 From bolometers to beetles: the development of thermal imaging sensors *Sensor Rev.* **27** 278–81

[175] Putley E H 1970 The pyroelectric detector *Semiconductors and Semimetals* ed R K Willardson and A C Beer (New York: Academic) pp 259–85

[176] Muralt P 2001 Micromachined infrared detectors based on pyroelectric thin films *Rep. Prog. Phys.* **64** 1339–88

[177] Hanson C M, Beratan H R and Belcher J F 2001 Uncooled infrared imaging using thin-film ferroelectrics *Proc. SPIE* **4288** 298–303

[178] Belcher J F *et al* 1998 Uncooled monolithic ferroelectric IRFPA technology *Proc. SPIE* **3436** 611–22

[179] Hanson C M, Beratan H R and Arbuthnot D L 2008 Uncooled thermal imaging with thin-film ferroelectric detectors *Proc. SPIE* **6940** 694025

[180] Hamrour M R and Galliou S 1994 Analysis of the infrared sensitivity of a quartz resonator application as a thermal sensor *IEEE Ultrasonics Symp.* vol 1 pp 513–6

[181] Hamrour M R, Galliou S and Dulmet B 1998 A new type of infrared-sensitive resonator used as a thermal sensor *Sensors Actuators* A **65** 147–51

[182] Kim Y and Vig J R 1997 Experimental results on a quartz microresonator IR sensor *Proc. IEEE Ultrasonics Symp.* pp 449–53

[183] Vig J R, Filler R L and Kim Y 1995 Microresonator sensor arrays *Proc. 49th IEEE Int. Frequency Control Symp.* pp 852–69

[184] Kao P and Tadigadapa S 2009 Micromachined quartz resonator based infrared detector array *Sensors Actuators* A **149** 189–92

[185] Willis J and Jimerson B D 1964 A piezoelectric accelerometer *Proc. IEEE* **52** 871–2

[186] Motamedi M E, Andrews A P and Brower E 1982 Accelerometer sensor using piezoelectric ZnO thin films *Proc. IEEE Ultrasonics Symp.* pp 303–7

[187] DeVoe D L and Pisano A P 2001 Surface micromachined piezoelectric accelerometers (PiXLs) *J. Microelectromech. Syst.* **10** 180–6

[188] Hui Y and Hang G 2007 Design of a bulk-micromachined piezoelectric accelerometer *Proc. IEEE Ultrasonics Symp.* pp 2598–601

[189] Zou Q *et al* 2008 Single- and triaxis piezoelectric-bimorph accelerometers *J. Microelectromech. Syst.* **17** 45–57

[190] Gerfers F, Kohlstadt M, Bar H, He M-Y, Manoli Y and Wang L-P 2007 Sub-ug ultra-low-noise MEMS accelerometers based on CMOS-compatible piezoelectric AlN thin films *Proc. Solid-State Sensors, Actuators and Microsystems Int. Conf., TRANSDUCERS 2007* pp 1191–4

[191] Aoyagi S *et al* 2007 Surface micromachined accelerometer using ferroelectric substrate *Sensors Actuators* A **139** 88–94

[192] Beeby S P, Ross J N and White N M 2000 Design and fabrication of a micromachined silicon accelerometer with thick-film printed PZT sensors *J. Micromech. Microeng.* **10** 322–8

[193] Hindrichsen C C, Thomsen E V, Lou-Moller R and Bove T 2006 MEMS accelerometer with screen printed piezoelectric thick film *Proc. IEEE Sensors Conf.* pp 1477–80

[194] Nemirovsky Y *et al* 1996 Design of novel thin-film piezoelectric accelerometer *Sensors Actuators* A **56** 239–49

[195] Wang L P *et al* 2002 Microelectromechanical systems (MEMS) accelerometers using lead zirconate titanate thick films *IEEE Electron Device Lett.* **23** 182–4

[196] Wang L-P *et al* 2003 Design, fabrication, and measurement of high-sensitivity piezoelectric microelectromechanical systems accelerometers *J. Microelectromech. Syst.* **12** 433–9

[197] Yu H G *et al* 2003 Lead zirconate titanate MEMS accelerometer using interdigitated electrodes *Sensors Actuators* A **107** 26–35

[198] André B *et al* 1992 Thin film PVDF sensors applied to high acceleration measurements *Sensors Actuators* A **33** 111–4

[199] Benech P, Chambered E and Monllor C 1996 Acceleration measurement using PVDF *IEEE Trans. Ultrason. Ferroelectr. Freq. Control* **43** 838–43

[200] Daku B L F, Mohamed E M A and Prugger A F 2004 A PVDF transducer for low-frequency acceleration measurements *ISA Trans.* **43** 319–28

[201] Marat-Mendes R, Dias C J and Marat-Mendes J N 1999 Measurement of the angular acceleration using a PVDF and a piezo-composite *Sensors Actuators* A **76** 310–3

[202] Marcal R F M, Kovaleski J L and Suzim A A 1997 A poly vinylidene fluoride (PVF_2) piezoelectric film based accelerometer *Proc. IEEE Instrumentation and Measurement Technology Conf., 'Sensing, Processing, Networking'* pp 908–13

29

[203] Spineanu A, Benabes P and Kielbasa R 1997
Digital piezoelectric accelerometer with
sigma-delta servo technique *Sensors Actuators*
A **60** 127–33

[204] de Reus R, Gullov J O and Scheeper P R 1999 Fabrication
and characterization of a piezoelectric accelerometer *J.
Micromech. Microeng.* **9** 123–6

[205] Senturia S D 2001 *Microsystem Design* (Boston, MA:
Kluwer Academic) p 689

[206] Levinzon F A 2004 Fundamental noise limit of piezoelectric
accelerometer *Sensors J. IEEE* **4** 108–11

[207] http://www.analog.com/static/imported-files/data_sheets/
ADXL335.pdf

[208] Madni A M and Wan L A 1998 Microelectromechanical
systems (MEMS): an overview of current state-of-the-art
Proc. IEEE Aerospace Conf. pp 421–7

[209] Madni A M, Wan L A and Hammons S 1996 A
microelectromechanical quartz rotational rate sensor for
inertial applications *Proc. IEEE Aerospace Applications
Conf.* pp 315–32

[210] Madni A M, Costlow L E and Knowles S J 2003 Common
design techniques for BEI GyroChip quartz rate sensors
for both automotive and aerospace/defense markets
Sensors J. IEEE **3** 569–78

[211] Eloy J C, Mounier E and Roussel P 2005 Status of the inertial
MEMS-based sensors in the automotive *Advanced
Microsystems for Automotive Applications 2005*
ed J Valldorf and W Gessner (Berlin: Springer)

[212] Madni A M and Geddes R D 2000 Micromachined quartz
angular rate sensor for automotive and advanced inertial
applications *Shock Vib. Dig.* **32** 51

[213] Bernstein J J *et al* 1997 Micromachined high frequency
ferroelectric sonar transducers *IEEE Trans. Ultrason.
Ferroelectr. Freq. Control* **44** 960–9

[214] Vernet J L, Steichen W, Lardat R, Garcia O and Gelly J F
2001 PMUTS design optimization for medical probes
applications *Proc. IEEE Ultrasonics Symp.* pp 899–902

[215] Muralt P 2005 Micromachined ultrasonic transducers and
acoustic sensors based on piezoelectric thin films
*Electroceramics-based MEMS: Fabrication-Technology,
and Applications* ed N Setter (New York: Springer)
pp 37–48

[216] Dogheche K *et al* 2005 Piezoelectric micro-machined
ultrasonic transducer (pMUT) for energy harvesting *Proc.
IEEE Ultrasonics Symp.* pp 939–42

[217] Percin G *et al* 1998 Micromachined two-dimensional array
piezoelectrically actuated transducers *Appl. Phys. Lett.*
72 1397–9

[218] Belgacem B, Calame F and Muralt P 2007 Piezoelectric
micromachined ultrasonic transducers with thick PZT sol
gel films *J. Electroceram.* **19** 369–73

[219] Wang Q *et al* 2006 Application of aluminum nitride thin film
for micromachined ultrasonic transducers *Materials
Research Society Symp. Proc.* pp 0892-FF13-01.1

[220] Akasheh F *et al* 2004 Development of piezoelectric
micromachined ultrasonic transducers *Sensors Actuators*
A **111** 275–87

[221] Jiang X, Snook K, Hackenberger W S, Yuan J R, Cheng A,
Schafer M and Geng X 2007 PC-MUT arrays for
ophthalmologic ultrasound *Proc. IEEE Ultrasonics Symp.*
pp 309–12

[222] Yamashita K *et al* 2002 Arrayed ultrasonic microsensors
with high directivity for in-air use using PZT thin
film on silicon diaphragms *Sensors Actuators* A
97–98 302–7

[223] Yamashita K *et al* 2004 Ultrasonic micro array sensors using
piezoelectric thin films and resonant frequency tuning
Sensors Actuators A **114** 147–53